IADC-11-05
April 2013

Inter-Agency Space Debris Coordination Committee

CHARACTERIZATION OF EJECTA FROM HVI ON SPACECRAFT OUTER SURFACES

April 2013

Prepared by the IADC WG3 members

Action Item 26.1

Change Record

Issue / Revision	Date	Section	Change(s)	Contributors
0.1	2010.03.12	All	Issue of doc. V0.1 during WG Session 3.2 of IADC28	A. Francesconi J.C. Mandeville
0.9	2012.03.31	All	Issue of doc. V0.9 for review by WG3 Chairman and J.C. Mandeville (expert)	A. Francesconi
0.95	2012.05.04	All	Issue of doc. V0.95 for review by WG3 Chairman and discussion within WG3 plenary meeting. Comments by J.C. Mandeville (expert) and inputs from P. Krisko – S. Flegel (WG2) included	A. Francesconi
0.96	2012.05.16	All	Update to document for review by WG3 Chairman and WG3 discussion	E. Christiansen
1.0	2012.06.11	All	Update to document with inclusion of M. Higashide comments and issue of doc. V1.0	A. Francesconi

List of Contributors

Chapter	Contributor	Affiliation
1	A. Francesconi	ASI - CISAS
	M.Higashide	JAXA
	J.C. Mandeville	CNES
	S. Meshcheryakov	ROSCOSMOS
	P. Krisko	NASA
	S. Flegel	TU Braunschweig - Institute of Aerospace Systems
2	A. Francesconi	ASI – CISAS
	J.C. Mandeville	CNES
	S. Meshcheryakov	ROSCOSMOS
3	A. Francesconi	ASI - CISAS
	J.C. Mandeville	CNES
	M.Higashide	JAXA
	E. Christiansen	NASA
4	A. Francesconi	ASI – CISAS
	J.C. Mandeville	CNES
	M.Higashide	JAXA
	E. Christiansen	NASA
	S. Meshcheryakov	ROSCOSMOS
5	A. Francesconi	ASI – CISAS
	J.C. Mandeville	CNES
	M.Higashide	JAXA

Table of Contents

List of Figures

List of Tables

Scope

The scope of this document is to summarize the knowledge available among WG3 members and the international community with respect to the production of backscattered ejecta from spacecraft outer surfaces as a consequence of hypervelocity impact of space debris and micrometeoroids.

This includes (1) consideration and models of ejecta effects on spacecraft subsystems and space environment pollution; (2) experimental results from WG3 members and recommendations for implementing experimental and numerical investigations on secondary debris production and (3) description of the structure of an ejecta database that could be regularly updated as new data become available.

Summary

In addition to the damage imparted to structures and internal components, space debris and micrometeoroids hitting external spacecraft surfaces produce a large amount of fragments that are ejected towards space. Such particles are named ejecta or secondary debris; they contribute to the environment pollution and are potentially harmful for nearby spacecraft parts, especially in case of grazing impacts.

Knowledge of the ejecta distribution is therefore important for both predicting the debris growth into the environment and for assessing the risk posed by secondary debris to spacecraft components. Moreover, a better understanding of ejecta production mechanisms could help in mitigating the secondary debris population, e.g. by a careful selection of surface materials that still obey all design requirements.

In order to address such issues, this report summarizes the available knowledge on ejecta as emerges from an extensive literature review, and provides indications on experimental and numerical methods that could be followed to obtain, analyze and organize new data on ejecta production.

The ejecta phenomenon is presented in Section 1 (Introduction), in which some relevant definitions are provided and the consequences of the secondary debris population are discussed, both in terms of environment contamination and damage induced to spacecraft. Furthermore, the orbital evolution of ejecta clouds is addressed.
Section 2 (Ejecta models) discusses the physical mechanisms behind ejecta production and presents common empirical models used to depict ejecta clouds, with special attention to the mass/speed distribution of secondary debris and its dependence from primary impact conditions. Consideration is also given to numerical approaches employed to simulate the very early stages of ejecta production and evolution.
Section 3 (Experimental activity by WG3 member agencies) contains a review of WG3 members recent activities to study secondary debris.
In Section 4 (Recommendations for experimental characterization of ejecta), indications are given on significant parameters to be measured for describing ejecta production mechanisms. Moreover, target materials and setup are recommended to represent realistic spacecraft configurations and suitable impact test conditions are proposed with reference to two benchmark cases useful to establish a common reference for comparing results obtained by different test facilities. Procedures for data utilization are suggested as well.
Section 5 (Ejecta database), a database structure is proposed to provide users with data concerning the behavior of material upon HVI with respect to their ejecta-production capability. The database will initially be populated with public data and could be regularly updated as soon as new test or simulation results become available.

1 Introduction

All spacecraft in Earth orbit are exposed to the risk of impact with micrometeoroids and orbital debris (M/OD). Because of the large collision velocities, hypervelocity impacts (HVI) with M/OD may cause significant damage to various subsystems and components up to mission failure. Furthermore, a large amount of new particles are produced which in part travel into the spacecraft and in part are ejected towards the space. As regards this latter aspect, brittle materials hit at hypervelocity are of particular concern, because of their peculiar impact response and their wide use for large satellites surfaces exposed directly to the space environment.

Return of the solar arrays from Eureca and the Hubble Space Telescope (HST) showed damage features not observed on ductile targets: low fracture toughness and high yield strength result in a wide range of failure modes, including cracking, spall and shatter. Thus, a great number of fragments in a wide size range (e.g. 15-100 µm for the HST solar arrays) are likely ejected at high velocities and contribute in the potential degradation of the space environment.

1.1 Definitions

We define as **ejecta** or **secondary debris** the amount of matter produced during a primary HVI of a M/OD upon a given target, e.g. a spacecraft surface. Such matter can be ejected under liquid, solid or gaseous state and comes from both the projectile and the impacted sample. A first classification of secondary debris is based upon the direction of ejection (Fig. 1-1):

- **Back-scattered ejecta** are emitted towards the half-space from which the primary projectile was coming, i.e. they come back to space thus contributing to the environment pollution. However, in case of oblique impact, back-scattered ejecta can immediately hit external spacecraft parts close to the primary impact point. Impacts due to secondary particles are called secondary impacts;
- **Downrange ejecta** travel into the spacecraft interior and can damage internal components placed on their trajectory. Downrange ejecta are produced only when targets are thin enough for spall formation on the rear face or complete perforation. On thin targets, back-scattered debris are less important than downrange fragments, which normally represent the largest part of the total ejected mass [Schneider, 1997].

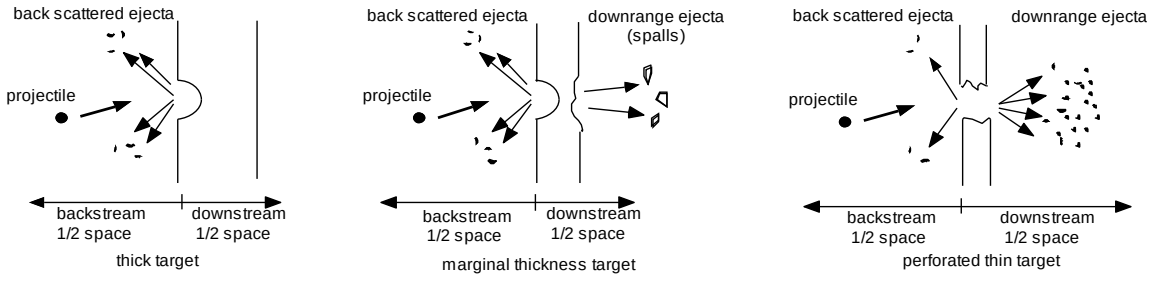

Fig. 1-1. Secondary debris produced during HVI: downrange ejecta, back-scattered ejecta

This report mostly deals with backscattered ejecta. With limitation to this case, Fig. 1-2 presents a sketch showing the ejection processes following normal as well as oblique impacts. This is useful to introduce some basic nomenclature on ejecta particles that are here divided into three different categories: jet fragments, cone fragments and spall fragments.

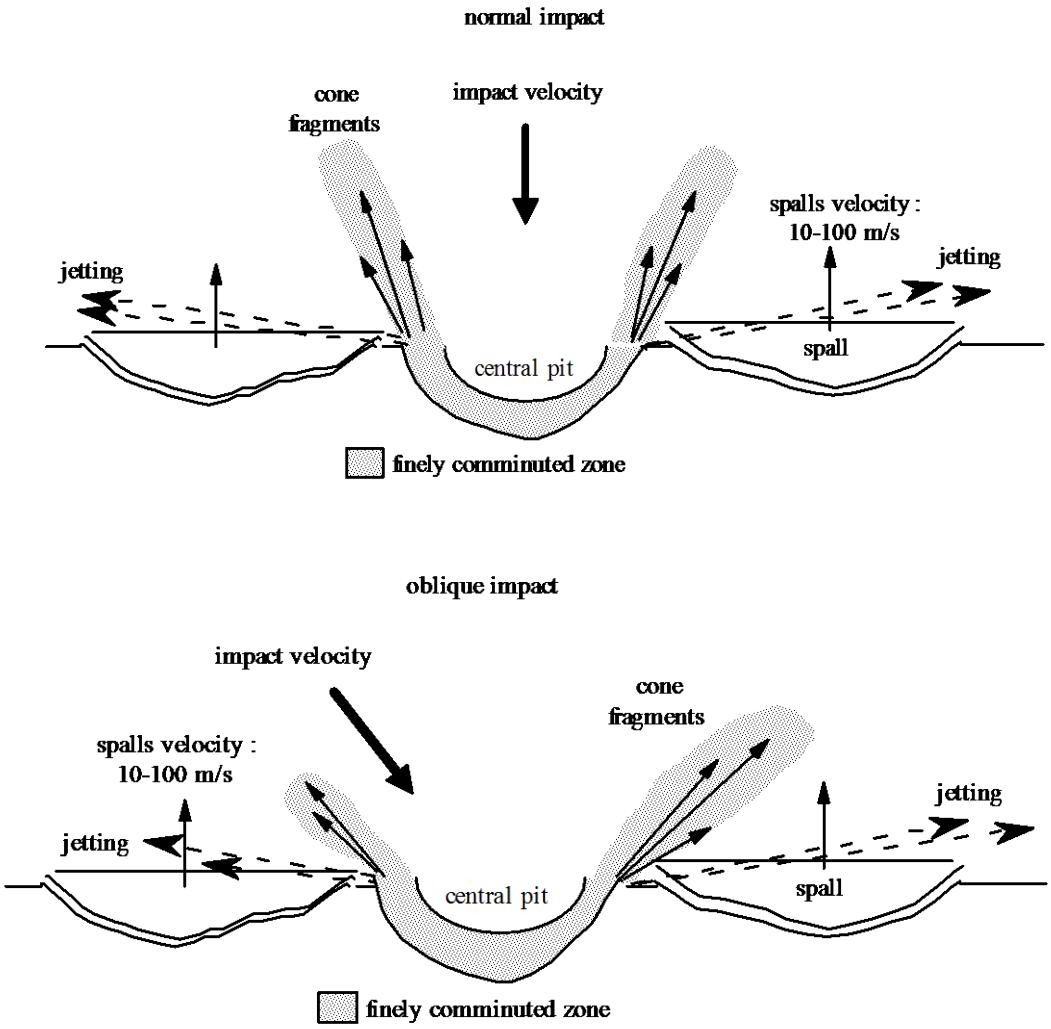

Fig. 1-2. Sketch showing ejection processes (jetting, cone, spall) after normal (top) and oblique (bottom) impact

1.2 Summary of international activities on ejecta

Secondary particles produced upon HVI on a target have been known since the beginning of HVI investigation, with initial attention given to material ejected from the surfaces of celestial bodies, such as the Moon and other planets. Early paper from Lecomte [1963] described the process, other works from Gault and Heitowit [1963], Gault et al. [1963, 1969, 1972] and Gault [1973] provided quantitative data concerning the amount and distribution of ejected particles from rocks and lunar materials. At the same time, it was suspected that secondary debris could contaminate sensors measuring solid particles fluxes on spacecraft.

Stump and Christiansen [1986] ran a series of light-gas gun (LGG) shots to determine empirical relationships for the size, mass, velocity and spatial distribution of spall and ejecta for targets representative of Space Station elements, with the objective of quantifying the threat posed by secondary debris to the station. They observed that the crater amount may be significantly increased with respect of what is calculated during the spacecraft design phase and proposed to consider the ejecta contribution as an additional flux over the primary one that is accounted for in the design process. They found from geometry considerations that secondary impact damage could concentrate in areas of station that are out-of-plane and trailing the majority of the modules. They suggested a 10% factor applied to the primary M/OD flux could account for secondary damage from ejecta.

Schonberg and Taylor [1990] developed recommendations to protect external spacecraft subsystems against damage by ricochet particles formed during oblique impacts. In the same framework, Schonberg [2001] reported empirical models describing the angles defining the spread of ricochet debris and the trajectory of the ricochet debris cloud center-of-mass as well as the velocity and diameter of the largest ejecta particle as a function of impact parameters and target plate geometry.

A first systematic review on ejecta phenomena was conducted under ESA contract by the University of Kent and ONERA/DESP in Toulouse [McDonnell et al, 1998], including a survey of the technical literature on secondary debris and the realization of some specific impact experiments. Furthermore, an analytical model was proposed to compute the amount of ejecta produced by HVI on selected target materials, such as aluminum alloys, solar cells cover glass and thermal control paint. A detailed description of the model and its use to predict the damage imparted by secondary particles on spacecraft is reported in [Rival and Mandeville, 1998], while the consequent generation of small orbital debris in space is discussed in [Bariteau and Mandeville, 2001]. The same ejecta model was later adopted by the ESA MASTER environment model and the ESABASE software.

CNES and CEA [Michel et al, 2005, 2006] conducted joint experimental and numerical studies on the ejection processes that occur during HVI on thin brittle targets, representative of solar cells and optics for space applications as well as instruments and laser optics employed in experimental activities relevant to nuclear research. In 2007, CNES and ONERA [Siguier and Mandeville, 2007] proposed within the Working Group 6 of ISO TC20/SC14 to set up a new standard concerning the space debris environment, with the aim of establishing a common test method to characterize the amount of ejecta produced by HVI on materials used on spacecraft outer surfaces. At the time of the first issue of this report, such standard was in the approval stage.

In the meantime, further independent investigations have been initiated by different institutions in countries belonging to the IADC. CISAS-University of Padova (Italy) conducted impact experiments to derive probability functions describing the number, size and speed distribution

of ejecta from three different targets representative of spacecraft materials, i.e. simple aluminum-alloy plates, silicon solar cells and simple aluminum-alloy plates covered by MLI blankets [Francesconi et al, 2010].

JAXA and KIT (Kyushu Institute of Technology) performed studies on ejecta characterization in support to the definition of the standard procedure ISO/CD 11227 to evaluate spacecraft material ejecta upon hypervelocity impact [Sugahara et al, 2009 – Mandeville et al, 2010]. Distribution of ejecta fragments were measured from craters in a witness plate, and a measurement process useful also for facility calibration was suggested.

Nagoya Institute of Technology (NIT) [Nishida et al, 2010] investigated the influence projectile density and target heat treatment on ejecta distributions. Craters in a witness plate were analyzed with a X-ray spectrometer to determine the structure of ejecta clouds, while size distribution of ejecta was obtained from fragments retrieved in the test chamber.

In Russia, a great deal of work has been made upon the ISTC 4312 Project [Shutov et al. 2010] to study many aspects concerning meteoroids and space debris. Hypervelocity impact tests were performed with emphasis on the collection of ejecta on soft witness plates. The evolution of ejecta clouds in near earth space was modeled in order to perform predictions on the future particles environment in orbit [Mescheryakov, 2009].

1.3 Damage to spacecraft induced by secondary debris

Damage to spacecraft parts in consequence of secondary debris impacts have been primarily investigated with respect to downrange ejecta, and extensive work on this point is available in the technical literature. Many studies have been performed to characterize the size and speed of secondary debris clouds expanding in the spacecraft interior after perforation of the external structure of the vehicle [Piekutowski 1987, 1990, 1993, 2001; Stilp et at 1990, 1997; Anderson et al 1990; Cohen 1995; Corvonato et al 2001], and several papers discuss the vulnerability of satellites internal components to secondary impacts (Melin 1990; Finnegan et al 1995; Lambert et al 1997; Paul 1997; Schaefer and Schneider 1997, Putzar et al 2008; Schaefer et al 2008].

On the other hand, back-scattered ejecta are usually very small particles (mainly sub-micron), with insufficient kinetic energy for producing damages as serious as those caused by downrange debris. However, in case of oblique impact, relatively large hypervelocity fragments can be generated and hit nearby spacecraft parts. Yet, typically backscattered ejecta does not have the capability of penetrating the completely through shielding or into the spacecraft body. Rather, they can trigger damage modes including the following:

- **Degradation of surface properties.** Solar cells, sensors, optics, MLI blankets and other thermal control coatings can suffer continuous degradation related to the production of impact craters, whose total area provides a measure of the degree of deterioration of the

surface. It is believed that secondary impacts have little effect on the transparency of solar panel glasses [Semkin et al, 2009], since degradation is mainly due to UV radiation and atomic oxygen. Optical systems of telescopes are instead more vulnerable.

- **Generation of false signals in photodetectors**. Stray pick-ups which can disturb the normal operation sensors can arise due to reflection of sun light by near passing particles [Mandeville et al, 2001]. Other false signals can be due to diffuse light flashes from secondary impacts on outer surfaces [Eichhorn, 1975, 1976; Semkin et al, 2009]. Impact flashes and light scattering can also disturb laser communication lines between satellites.
- **Electrostatic discharges**. Especially at low altitude, secondary debris can cause collective plasma effects which can lead to electric breakdowns between different spacecraft surfaces and/or solar arrays [Borisov et al, 2010; Korsun, 2010].
- **Disturbances to electronic boards**. Emission of microwave radiation is known to occur during HVI [Takano et al, 2000, 2002, 2005; Maki et al, 2002]. Distributed impacts of small particles clouds onto spacecraft surfaces can produce microwave emission strong enough to cause malfunctions in nearby electronic equipment [Caswell et al, 1995; Mc Donnell et al, 1997].
- **Penetration of lightly protected or thin materials such as EVA suits**. Thin materials on spacecraft and space suits used for extravehicular activity (EVA) are susceptible to penetration by small ejecta and M/OD particles. For instance, the Shuttle space suit gloves are relatively thin to increase dexterity of the glove, and hypervelocity particles on order of 0.2mm diameter (aluminum) can penetrate through the outer cover and inner bladder of the fingers [Christiansen et al, 1999]. Some of the ejecta particles produced in M/OD impacts would be capable of penetrating the EVA suit under typical impact conditions for debris in low Earth orbit; see for example the ejecta fragment size produced in experiments described in this report such as Fig. 3-10 and Fig. 3-18.

It is clear that backscattered ejecta can represent a threat for current and future space missions, since they can contribute to the deterioration of specific surface properties, interfere with scientific measurements, disturb electronic boards, as well as cause serious mechanical damage to thin membranes used for solar sailing or aerodynamic de-orbiting of spacecraft. It is therefore important to better understand the extent of the secondary debris phenomenon, in order to define strategies for reducing the risk posed to future missions.

1.4 Environment pollution

Downrange secondary debris can remain trapped within the satellite, or leak out into the space environment over time via hole or gaps in the spacecraft outer structure. Backscattered ejecta, on the other hand, are emitted directly to the free space around the spacecraft, adding to the environment thus increasing the number of existing debris. If backscattered ejecta are not stopped by a surface on the satellite close to the primary impact point, they escape from the vicinity of the parent vehicle and are injected into the environment on their own orbital trajectory. Depending on their size and orbital parameters, they can have long lifetimes on orbit and strike other spacecraft at large distance or re-enter rapidly in the atmosphere.

Backscattered ejecta are currently modeled and provided to the general public by two space agencies, ESA and NASA, within orbital debris engineering models, MASTER and ORDEM, respectively. Each group follows a unique approach in the derivation of these populations.

For the ESA-MASTER-2009 model, ejecta are provided in quarterly population snapshots for the years 1957 to 2055. Ejecta are simulated by calculating the debris flux onto all payloads and rocket bodies. The resulting impacts are evaluated based on the equations by Rival and Mandeville [Rival and Mandeville, 1999]. Only cone and spall ejecta are taken into account as only about 1% of the ejected mass are produced by jetting. The resulting ejecta population is validated by comparing the simulated flux onto LDEF, the Hubble-Space Telescope and EuReCa to measurement data from the retrieved surfaces.

The NASA model ORDEM 3.0 contains yearly degradation/ejecta populations (2010-2035), of sizes 10μm to about 1mm. The principal data used are in-situ hypervelocity impact records that are accumulated in over 30 post-flight damage surveys of NASA Space Shuttle radiator panels and window panes [Xu et al, 2011]. Populations are derived based on varying the production rate of degradation/ejecta from large resident space objects (>10cm), and reconstructing the hypervelocity data.

In summary, it is believed that ejecta contribution to the orbital debris population cannot be neglected, being of about 2-3% in LEO and 5-6% in GEO [Siguier and Mandeville, 2007].

The regions of geostationary and high elliptical orbits are the most prone to experience pollution by ejecta [Kessler, 1990; Kolesnikov and Chernov, 2009]. Here, debris is resident for a long time and many spacecraft are present that can be a source of new fragments.

Special attention should be given to ejecta in the **geostationary region**. Among the long orbital lifetime, it must be considered that the average power of spacecraft in GEO is high (the total power is ~1.8 MW) and therefore the total solar arrays area is relevant (~20'000 m^2). Due to the brittle nature of the materials involved, the mass of spall fragments coming from solar cells cover glass can be three orders of magnitude larger than that of the impactor [Rival et al, 1996]. Results of the analysis of servicing missions on the HST solar arrays show that ~0.02 g/m^2 of ejecta can be generated per year [Moussi et al, 2005] and thus a production of ~400 g/year of glass fragments can be predicted in GEO. Such particles spread over a large volume and it could be expected that critical levels of secondary debris would be reached in the near future even though the average ejecta flux is currently two orders of magnitude lower than that of meteoroids (~30 particles/year/m^2 compared to ~4000 particles/year/m^2) [Oswald et al, 2005]. In fact, ejecta continue to pollute the GEO region even after the parent vehicle has been moved to a disposal orbit. At present, the belt of microparticles in GEO is already visible by space based optical or infrared sensors [Drolshagen et al, 2009].

Even in the case of **high elliptical orbits**, the flux of ejecta fragments crossing the LEO region is

about half of the total debris flux [Kessler et al, 1996].

1.5 Orbital evolution of ejecta

Knowledge of ejecta orbital evolution is important not only for estimating the secondary debris contribution to the environment, but also for defining test methods and instrumentation needed for ejecta characterization. In fact, sensitivity as well as resolution of recommended experimental techniques should be adapted to those particles that contribute significantly to the OD fluxes.

Backscattered ejecta can remain for a long time at altitude greater than ~1000 km where drag is negligible. The solar radiation pressure and various gravitational disturbances are conservative and therefore tend to redistribute the ejecta between different regions of the space instead of facilitating their de-orbiting. As a consequence, secondary debris are inclined to accumulate in some orbital regions and form ejecta belts [Kessler and Cour-Palais, 1978; Drolshagen et al, 2009] and even the formation of temporary clusters of small particles becomes possible [Myagkov, 2009].

Orbital evolution of ejecta has been studied to some extent by Bariteau and Mandeville (2001) and Bariteau (2001), with special attention to GTO and LEO regions. In particular, a simplified analytical model has been derived [Mandeville and Bariteau, 2004]. Shutov et al (2010) describe in detail the orbital evolution of ejecta produced by primary meteoroid impacts on the solar arrays of the ISS.

In the case of ORDEM, degradation/ejecta produced from large resident space objects are propagated in orbit accounting for standard perturbative forces, J2, J3, J4, solar-lunar gravity, solar radiation pressure with Earth shadow, and atmospheric drag based on Jacchia 77.

The evolution of the ejecta population of the MASTER-2009 model is predicted using a semi-analytical propagator. Zonal harmonics up to degree five, third body perturbations from the sun and moon, solar radiation pressure with cylindrical Earth shadow and atmospheric drag are taken into account. Atmospheric density calculation is based on the MSIS'77 model.

2 Ejecta models

This section provides a summary of models describing ejecta phenomena. Information refers to literature findings as well as specific activities carried out by WG3 members in the framework of the IADC AI 26-1 “Characterization of ejecta from HVI on spacecraft outer surfaces”.

Although no complete ejecta model is currently available, different empirical approaches are reported to predict the number, size, speed and direction of back-scattered secondary particles generated during a single hypervelocity impact, as a function of impact parameters and projectile properties.

Such models are mostly based upon impact test data collected in different and various conditions, while theoretical and/or numerical analysis to extend experimental data and/or address secondary effects (e.g. plasma) are less diffused.

2.1 Mechanisms involved in ejecta production

Although several and diverse phenomena occur to produce ejecta, investigations carried out so far are mostly limited to the physical state and distribution of the ejected particles (number, size, speed, direction). However, a few common elements emerge among the large variety of experimental and theoretical information available from the technical literature:

- Ejecta production is related to three main mechanisms which lead to the production of jet, cone and spall fragments (see Fig. 1-2). Jet fragments are small and fast particles emitted at grazing angles in the very early stages of impact (i.e. few microseconds); cone fragments are formed just after the completion of the jetting process and are small and fast particles emitted at constant elevation angle, creating a cone around the impact crater; spall fragments appear at later stages (i.e. tenths of microseconds), they are large particles ejected at low velocity perpendicularly to the impacted surface.
- The most important parameters influencing the ejection mechanisms are the impactor kinetic energy and incidence angle, and the ductile or fragile nature of the target.
- The thickness of the target relative to the projectile diameter is another important parameter influencing the mass and size of the ejecta particles. For targets that are completely penetrated, ejecta production and size are reduced as target thickness decreases.
- The total ejected mass, the number, size, shape, speed, direction and physical state of emitted particles are often considered for ejecta characterization. Models reported in the following refer to the aforementioned parameters, except for describing the effect of target thickness.

In contrast, secondary effects are rarely considered only when they could affect specific applications:

- Plasma clouds and impact flashes are formed around the primary impact crater, resulting in possible interference with sensitive equipment. Plasma generation is strongly dependent from the impact obliquity, with a significant enhancement for shallow angles.

2.2 Empirical models

This section summarizes available models describing ejecta particles in terms of:

- Total mass, physical state and mass partitioning between jet, cone and spall fragments
- Size and speed distribution
- Ejection angles.

Consideration is also given to experimental data used for models derivation.

2.2.1 Total mass of ejecta fragments

The bulk of the total ejecta mass is in solid state within cone and spall fragments. In few experimental cases, evidence of liquid ejecta was provided by the presence of re-solidified droplets ("splashes"). However, no experimental measurements of the liquid (and/or gaseous) amount of matter can be found in the literature.

a. Total ejecta mass

Measurement of the total ejected mass $M_{e,tot}$ is usually done by collection and weighing of ejected fragments, which is compared to target mass loss. Most authors try to relate $M_{e,tot}$ to the impact kinetic energy E_k :

$$M_{e,tot} = C \cdot E_k^A \cdot \cos^2 i \qquad \text{Eq. 2-1}$$

C and A are experimental coefficients depending from the projectile and target materials, i is the impact angle (i=0° means normal impact). Values for C and A are given in Tab. 2-1, according to experiments carried out by different authors.

Author	*Target*	A	C
Gault and Heitowit, 1963	Sand, rocks	1.0	1.25E-5
Dohnanyi, 1967	Basalt	1.0	1.0E-5
Gault, 1973	Basalt	1.133	7.41E-6 $(\rho_p/\rho_t)^{1/2}$
Bess, 1975	Satellite wall	1.0	2.0E-5
Seebaugh, 1977	Soil	0.9	1.0E-4
Frisch, 1991	Ice	1.13	4.9E-5
Woodward et al, 1994	Ceramics	1.0	0.9E-5

Tab. 2-1. Values for C and A coefficients in Eq. 2-1 (SI units). ρ_p and ρ_t are the projectile and target density

C and A values obtained by Gault and Heitowit (1963) are based on hypervelocity impacts on sand and various rocks, on low-velocity impacts, and on chemical or nuclear explosion craters. Dohnanyi (1967) used the same experimental data for deriving specific values of the C and A coefficients for basalt. The dependence of C from the projectile and target density was introduced by Gault (1973), using hypervelocity impacts data on basalt and granite targets, with crater size ranging from 10 μm to 10 m; the influence of the impact angle was considered as well. Bess (1975) obtained values of the C and A coefficients using few satellite wall destruction tests (thin target case). Seebaugh's experiments refer to explosion in soil with craters larger than 10 m. Frisch's data show that the amount of matter ejected during hypervelocity impacts on icy targets could be 5 times larger than on rock targets. Data from Woodward and al. (1994) show that the amount of ejecta decreases when the fracture resistance K_{IC} of the target increases: the ejecta volume is halved when K_{IC} is doubled.

Some important information comes out from Eq. 2-1 and Tab. 2-1:

- **Total amount of the ejected matter**. From the values of coefficients C and A, it appears that $M_{e,tot}$ is much larger than the projectile mass m_p, as soon as the hypervelocity regime is reached. For instance, the M_e/m_p ratio is about 250 for a 10^{-2}g projectile at 7 km/s velocity.
- **Influence of target material**. Most of the targets used in the experiments cited above are brittle (rocks, basalt, ice, ceramics) since very limited data are available as regards ductile targets. The amount of ejected matter during an hypervelocity impact on an icy target is 5 times larger than on a rock target. Material density is accounted for only in C coefficient suggested by Gault (1973).
- **Influence of impact angle**. In the case of oblique impacts, Gault (1973) observed that the total amount of ejected matter decreases when the incidence angle i increases. This can be due to the shallow profile of craters resulting from oblique impacts.

b. Mass partitioning between the 3 ejection processes

The total ejecta mass is partitioned between the three ejection mechanisms of jetting, cone and spallation:

$$M_{e,tot} = M_{jet} + M_{cone} + M_{spall} \qquad \text{Eq. 2-2}$$

Schneider (1975) and Eichhorn (1976) estimated that the mass ejected in the jet is about $\sim 10^{-6}$ and $\sim 10^{-4}$ of the projectile mass. This is very low compared to the total ejecta mass and hence it can be assumed that $M_{e,tot}$ is shared between cone and spall fragments only. The relative contribution of both processes depends on the impact crater size: spall fragments become more and more evident as craters size increases (Tab. 2-2).
However, it should be reminded that no spall formation is reported on ductile targets.

Author	*Target*	*Crater size*	$M_{spall}/M_{e,tot}$
Lange et al (1984)	Rock	1-10 cm	60-80%
Polanskey et Ahrens (1990)	Rock	1-10 cm	39-67%
Rival et al (1996)	Glass	10 μm	0
"	Glass	100 μm	>40%
"	Glass	1 mm	>60%
"	Solar cell	10 μm	0
"	Solar cell	100 μm	>40%
"	Solar cell	1 mm	90%

Tab. 2-2. Mass partitioning between cone and spall fragments

Special attention should be given to solar cells, whose multilayer structure of solar cells prepares for large cracks propagation and delamination at interfaces. Fig. 2-1 [Rival et al, 1996] shows a cross-section view of an impact on a solar cell from the HST arrays left) and a schematic representation of spall phenomenon due to delamination (right). As a consequence, the mass ejected trough spallation is relatively larger than on a brittle homogeneous surface. Examination of HST solar cells performed by Rival et al. (1996) highlighted that the spall mass could reach 90% of the total ejected mass for mm-sized impact craters.

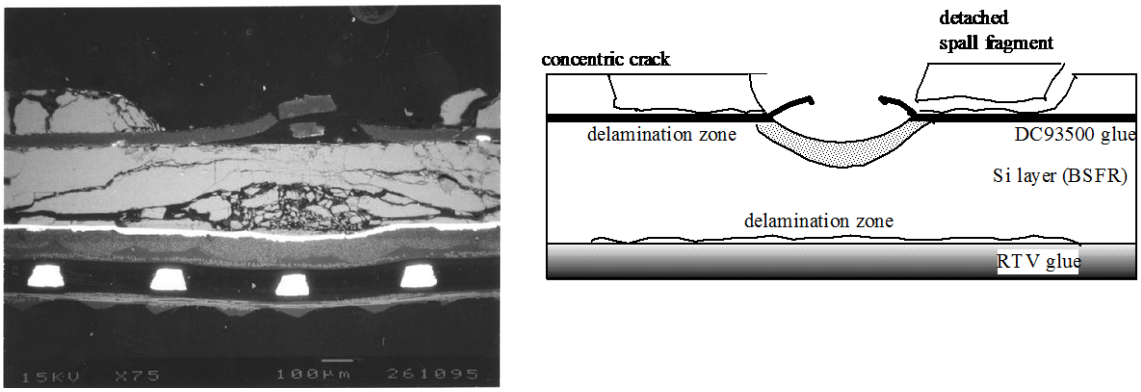

Fig. 2-1. Cross-section view of an impact crater on HST solar arrays cover glass (left), showing delamination cracks and large ejected spalls. Solar cell schematic (right) [Rival et al, 1996]

2.2.2 Size and speed distribution of fragments

a. Size distributions

Many experiments were devoted to fragment size estimation, in order to derive empirical distribution laws. A variety of measurement techniques were used, e.g. sifting, secondary craters study and pictures analysis. Most authors agree on a power-law distribution for ejecta size:

$$n(\delta)d\delta = \delta^{\alpha} d\delta \qquad \text{Eq. 2-3}$$

Where $n(\delta)\, d\delta$ is the number of fragments of size (mean diameter) between δ and $\delta+d\delta$, and α is

the exponent of the cumulative distribution. Other important parameters define the lower (cut-off) and upper limits of fragments described by the power-law distribution

Other important parameters are the largest and the smallest (cut-off) fragment mass. Tab. 2-3 provides a summary of parameters for power-law size distributions according to different authors.

Author (comment)	*Target*	α	*Cutoff*	*Upper limit*
Gault, 1973 (spall fragments excluded)	Basalt	-3.7 to -3.3 -3.6 nominal	0.1 μm	$0.1M_{e,tot}$ or $0.2M_{e,tot}^{0.8}$ or 10-100 m_p
Dohnanyi, 1967	Balsalt	-3.4		$0.1M_{e,tot}$
Asada, 1985	Basalt Copper Ice	-3.5 -3.0 -2.5 to -2.0	0.1 μm	100 μm
Fujiwara et al, 1977, 1980	Gypse	-3.47		
Lange et al, 1984 (only spall fragments)	Rock	-2.8 to -2.5		
Frisch, 1991 (only spall fragments)	Ice Basalt, granite	-2.75 -3.5 to -2.6		
Barge and Pellat, 1993 (non destructive impacts) (destructive impacts)	Various	 -3 -4		
Bess, 1975 – McKnight, 1991 – McKnight and Edelstein, 1992 (satellite wall)	Hard metal Soft metal	-3.66 to -3.4 -2.2		
Cour-Palais, 1982	Graphite-epoxy Aluminum alloy	-5.26 to -4.48 -4.48 to -3.88		
Seebaugh, 1977	Soil	-3.5		
Eichhorn, 1975, 1976	Gold			2-3 m_p

Tab. 2-3. Power-law size distribution of ejecta according to different authors

However, authors note a discrepancy between experimental measurements and power-law distribution predictions at the smallest and largest ejecta diameters. For smallest sizes, predictions over-estimate the number of fragments. This could be due, on one hand, to the experimental detection limits and, on the other hand, to the physically natural roll-off of the distribution when the cut-off size is approached. For largest sizes, experimental measurements are disturbed by spall fragments, whose formation is different from cone fragments, and this introduces additional discrepancy. McKnight (1991) proposed other distribution functions with more degrees of freedom (parabolic or hyperbolic functions): this gives a better data fitting but the various coefficients do not have any physical significance.

Additional comments on the power-law distribution validity:

- **Influence of target material**. O'Donnell (1991) and Woodward et al (1994) experiments on ceramics targets showed that increasing the materials fracture toughness K_{IC} results in

increasing the relative fraction of small fragments.

- **Influence of impact velocity**. Starting from the experiments of Bess (1975) and McKnight (1991), it was shown that the fraction of small fragments increases when impact kinetic energy increases. This is confirmed by O'Donnell (1991) and Woodward et al (1994) results on ceramics. This can be explained by a more significant number of activated micro-cracks in the target.
- **Oblique and grazing impacts**. Schonberg (1989) showed of a relative increase of fragments size (large particles are more numerous) for grazing impact incidence. This can be explained on one hand by a tearing effect on the target (shearing) and, on the other hand, by incomplete destruction of the projectile. For oblique, but non-grazing impacts, the size distribution of fragments is similar to the one obtained from normal impacts.
- **Distinguishing between spall and cone fragments**. The number of spall fragments is small and their size is usually large (at least projectile size). However, spall fragments can also break after ejection, because of residual stress or collision with other fragments. They usually have a plane side because they are generated near the target free-surfaces. Cone fragments are much smaller and much more numerous. They come from target disruption near the primary crater.

b. Speed distributions

Experimental measurement of ejection velocity is complex: in most cases, only maxima and minima velocities are estimated. However, there is a consensus on the inverse relation between secondary particle size and its ejection velocity: smallest fragments are the fastest and largest ones are the slowest. Spall fragments velocities are clearly distinct from cone and jet particles, while smallest cone fragments and jet particles have similar ejection velocities, and some authors do not state precisely whether the maximal ejection velocity refers to a jet or a cone particle. Tab. 2-4 gives a summary a various velocity measurements for different projectile velocities v_p.

Author	*Target*	v_p *(km/s)*	*Jet (km/s)*	*Cone (km/s)*	*Spall (km/s)*
Schneider, 1975	Rock	4.1	> 3		
Gault et al, 1963	Basalt	6.4	Max $3v_p$	$\sim v_p$	<0.1 0.01-0.1v_p
Eichhorn, 1976	Gold	5.0	~ 30		
Frisch, 1991	Ice	1.8-9.6			0.004-0.57
Arakawa et al, 1995	???	0.03-0.5			<0.01
Polanskey and Ahrens, 1990	Rock	1.7-6.5			0.001-0.03
Woodward et al, 1991	Ceramics	1.0			0.15-0.25
Asada, 1985	Basalt	4.0	~ 10	>1 (average)	~ 0.1
Christiansen, 1987	Aluminum alloy	6.45		6.7 (max)	

	35%SiC-Al alloy	6.71		5.2 (max)
	Al mesh	6.50		2.1 (max)
Lecomte, 1963	Aluminum alloy	5.0	3.8-5.7	0.47-1.05
Stoffler et al, 1975	sand	6.5		0.2
Schonberg, 1989	Aluminum alloy	5.0-7.5		0.5-10

Tab. 2-4. Ejecta speed as function of projectile velocity v_p according to different authors

Additional comments:

- **Influence of impact velocity**. Gault et al (1963), Eichhorn (1976) and Polanskey and Ahrens (1990) showed that the fastest fragments velocities (jet particles and small cone fragments) are directly related to impact velocity. On the contrary, spalls ejection velocity is not very sensitive to impact speed variations
- **Oblique and grazing impacts**. Svedhem and Pedersen (1992) showed a slight dependence of the jet particles velocity on angle of incidence : maximal ejection velocity appeared to increase as impact obliquity increases. In the case of grazing impact, Schonberg (1989) measured higher velocities for cone fragments, from 500 m/s for largest ejecta to 10 km/s for smallest ones. Similar tests performed at EMI [Schneider and Stilp 1993] evidenced that jet particles velocities could reach 2 to 3 times the primary impact speed: this was attributed to the plasma cloud generated in the early phases of impact which accelerates the smallest jet particles [Schneider, 1997].

c. Coupled size-speed distributions

Most authors agree on the inverse dependence between ejecta size and ejection velocity. However, it should be considered that fragments speed can be modified just after ejection by collisions inside the ejecta cloud.
Precise measurement of individual fragment velocities is currently unfeasible. In the remainder of this section, two semi-empirical models exist to describe the coupled size-speed distribution of fragments are reported.

- **O'Keefe and Ahrens** (1987) proposed the following mass-velocity empirical model from Gault experimental results and additional numerical simulations:

$$f(m,v) = 1 - \left[\frac{m}{m_{bv}(v)} \right]^{1/6}$$

$$m_{bv}(v) = m_b \left(\frac{v}{v_{\min}} \right)^{-3}$$

Eq. 2-4

In the above formulas, $f(m,v)$ is the cumulative number of fragments with mass larger than m and ejection velocity equal to v, $m_{bv}(v)$ is the mass of the largest fragment ejected at velocity v, m_b is the mass of the heaviest fragment (given by the Gault equation $m_b = 0.2M_{e,tot}^{0.8}$, see Tab. 2-3) and v_{min} in the minimum velocity in the ejecta cloud.

- **Su (1990)** combined the Bess (1975) size distribution model for collision fragments and a specific function to derive ejection velocity from ejecta size and impact parameters. The model refers to catastrophic collisions (i.e. satellite destruction) rather than individual micro-impacts. It was adopted by several authors (McKnight 1991, Hill 1990) and has been used in NASA orbital debris environment models [Kessler et al, 1996]:

$$\log\frac{v}{v_P} = \begin{cases} A + B\log^2\dfrac{\delta}{\delta_m} & if\ \ \delta \geq \delta_m \\ A & if\ \ \delta < \delta_m \end{cases} \qquad \text{Eq. 2-5}$$

$$\delta_m = \frac{E_k^{1/3}}{C}$$

In the above formulas, v_p is the projectile velocity, δ is the fragment diameter and E_k is the projectile's kinetic energy (J). A, B and C values are 0.2225, -0.1022 and 6.194E7 in the high velocity regime, and -0.9090, -0.0868 and 1.347E7 in the low velocity regime (yet, the author does not provide any criterion for distinguishing between the two velocity ranges).
For very energetic impacts, the $\delta < \delta_m$ condition is always true, therefore all fragments are ejected at the same velocity. However, to account for velocity differences at a given fragment size, an artificial scattering is suggested: 50% of the fragments have speed equal to the exact v value given by Eq. 2-4, 20% have speed equal to $0.6v$, 20% have speed equal to $1.4v$, 5% have speed equal to $0.2v$ and 5% have speed equal to $1.8v$.

2.2.3 Ejection angles

Fragments ejection directions can be described in terms of elevation (angle between the velocity vector and the target plane) and azimuth (angle between the velocity vector projection on the target plane and a reference axis in the same plane). However, most authors focus on the elevation only (Fig. 2-2), while very few data are available on oblique impacts and consequent azimuth variations of ejection directions.

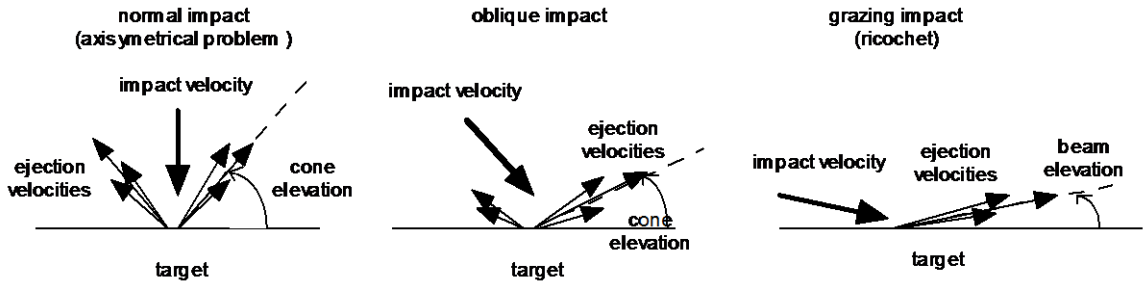

Fig. 2-2. Schematic representation (cross-section view) of debris cone for normal impact (left), oblique impact (center), and grazing impact (right).

Fragments ejected in the 3 processes (jetting, cone, spall) can be distinguished by their elevation angle. Formation of the debris cone is evidenced in all cases. It consist of a great number of fragments ejected at nearly the same elevation, which gives a conical aspect to this debris cloud (cone centered at impact point, with an axis perpendicular to the target plane (Fig. 2-2, left). Cone elevation angles measured by several authors are reported in Tab. 2-5. It should be noted that the cone angle is not constant. During the impact process, as the projectile first contacts the target, the cone angle (elevation angle) is at its minimum value. But as the projectile penetration deepens into the target, the cone angle (elevation angle) increases to its maximum value. Spall fragments typically are ejected normal to the target, whereas the jets occur at very low angle relative to the target.

Author (comment)	*Target*	*Projectile*	*Jet (°)*	*Cone (°)*	*Spall (°)*
Schneider, 1993	Glass	Steel	20	60-70	
Gault et al, 1963	Basalt	Aluminum	<40	40-60	80
Asada, 1985	Basalt	Nylon	10-40	45-55	90
Oberbeck and Morrison, 1976	Sand	Plastic		35-40	
Stoffler et al, 1975	Sand	Plastic		35-50	
Frisch, 1991	Ice	Glass			90
Eichhorn, 1976	Gold	Iron, Carbon	>20	50-70	
Christiansen, 1987	Al alloy 35% SiC – Al alloy	Aluminum Aluminum		64 (max) 63 (max)	
Lecomte, 1963 (v_p=3.5 km/s) (v_p=7 km/s)	Al alloy	Polyethylene	 50 80	 40 50	
Svedhem and Pedersen (1992)	Gold	Iron		60	
Polanskey and Ahrens, 1990	Rock	Various			90

Tab. 2-5. Ejecta elevation angles according to different authors

Additional comments:

- **Influence of projectile and target material**. The cone elevation is related to crater depth: for a relatively deeper primary crater, the fragments are guided in a more perpendicular direction, therefore the cone elevation increases. Crater depth depends highly on the ρ_p/ρ_t ratio: the larger the relative projectile density is, the deeper the crater is. It is also possible to find very deep craters on high density, but highly ductile targets, such as gold.
- **Influence of impact velocity**. Increase of elevation angle with increasing impact velocity can also be explained by primary crater shape, which becomes deeper with increasing impact velocity. This influence is less important on brittle targets.
- **Oblique and grazing impacts**. The influence of impact incidence on shape and opening of the cone has been studied by Svedhem and Pedersen (1992). They found that cone elevation decreases for oblique impacts (flattening of cone) and the relative amount of ejected mass is increased in the downrange azimuth direction (distortion of cone). Schonberg (1989) performed tests at grazing incidence (less than 25° elevation), showing that fragments are no longer ejected in a cone around an axis perpendicular to the target, but in a conical beam centered on an axis of about 15° elevation and parallel to the impact azimuth direction. This conical beam is concentrated within a few degrees of elevation aperture, while it has a larger azimuth scattering. This phenomenon is often called "ricochet" (Fig. 2-2, right).

2.3 Numerical simulations

Numerical simulation of ejecta phenomena have been mainly performed referring to impacts of asteroids on planet-like celestial bodies, while limited consideration has been given to production of secondary fragments from HVI on spacecraft surfaces.

In the framework of the ASI “Space Debris Program”, hydrocodes calculations were carried out by CISAS-University of Padova with the aim of reproducing the ejecta distribution resulting from specific impact experiments on satellite materials (see test program in the following section 3.1).

Two tests (no.8648 and no.8657, see Tab. 3-1) were selected as benchmark for normal and oblique impact on aluminum alloy targets and the comparison between experimental results and numerical simulations were performed referring to the damage pattern resulting on 2 mm thick copper witness plates located close to the primary target. Simulations were carried out using Ansys-Autodyn 2D and 3D for normal and oblique impacts respectively (Fig. 2-3 and Fig. 2-4).

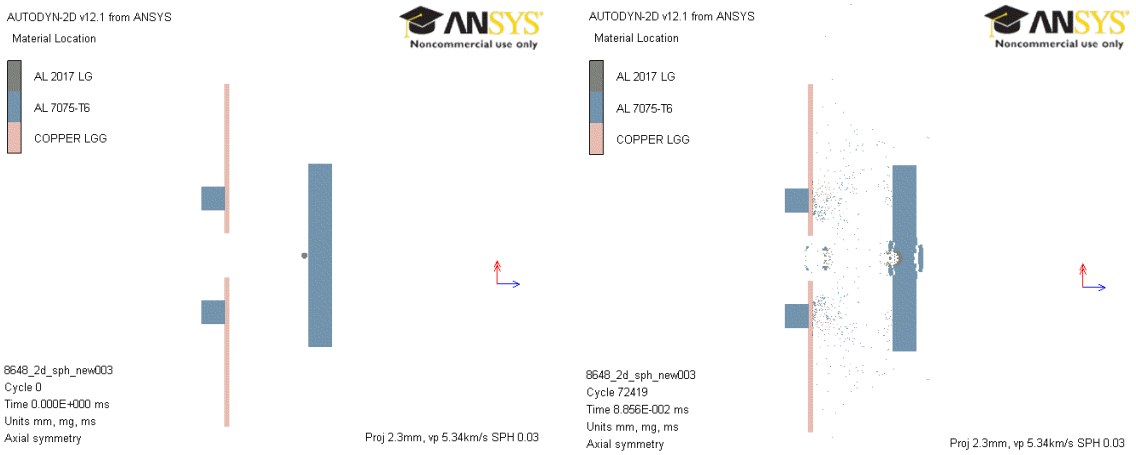

Fig. 2-3. Numerical simulation of the ASI-CISAS test no.8648 (d_p=2.3 mm, v_p=5.34 km/s, normal impact)

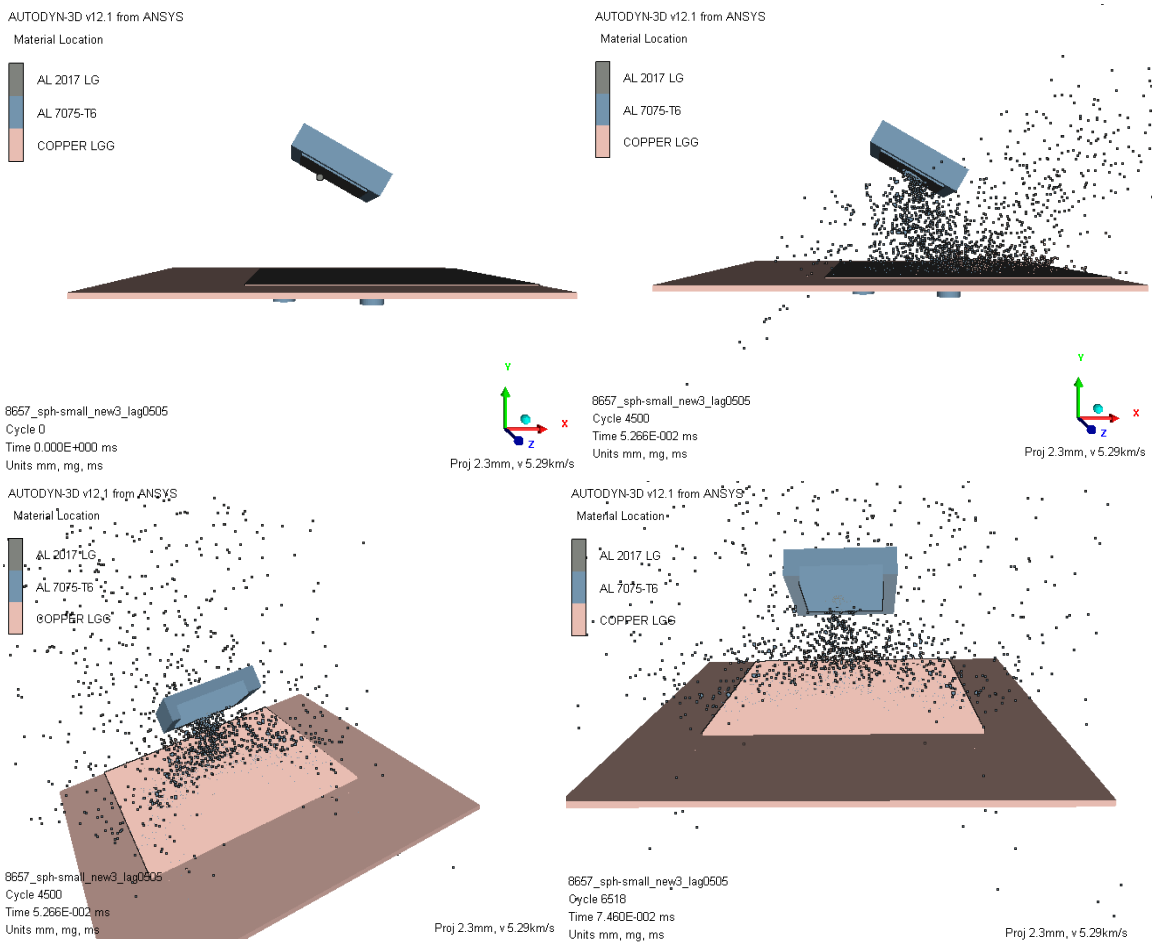

Fig. 2-4. Numerical simulation of the ASI-CISAS test no.8657 (d_p=2.3 mm, v_p=5.29 km/s, α=60°)

In the first case (test no.8648, 2D-axial symmetry), SPH meshes with two different resolutions (i.e. 0.03 mm and 0.5 mm) were used for both the projectile, the target and the witness plate. The highest resolution is similar to that achievable from real witness plates crater measurements, but led to a significant computational burden. On the other hand, the lowest resolution does not allow prediction of witness plate craters in most of the range of interest and therefore only a raw assessment of the shape and size of the witness plate damage pattern was

possible.

In the second case (test no.8657, 3D), SPH were used only for the projectile, the target close to the impact point and the witness plate surface and a 40 mm resolution was set to further decrease the computational load. Furthermore, it was necessary to stop the simulation when the ejecta cloud was still evolving.

Considering the above limitation, a comparison between experimental and numerical results was performed as regards the global extension of the ejecta cloud footprint on the witness plates, according to the parameters described in Fig. 2-5. Results are presented in Tab. 2-6 (normal impact) and Tab. 2-7 (oblique impact).

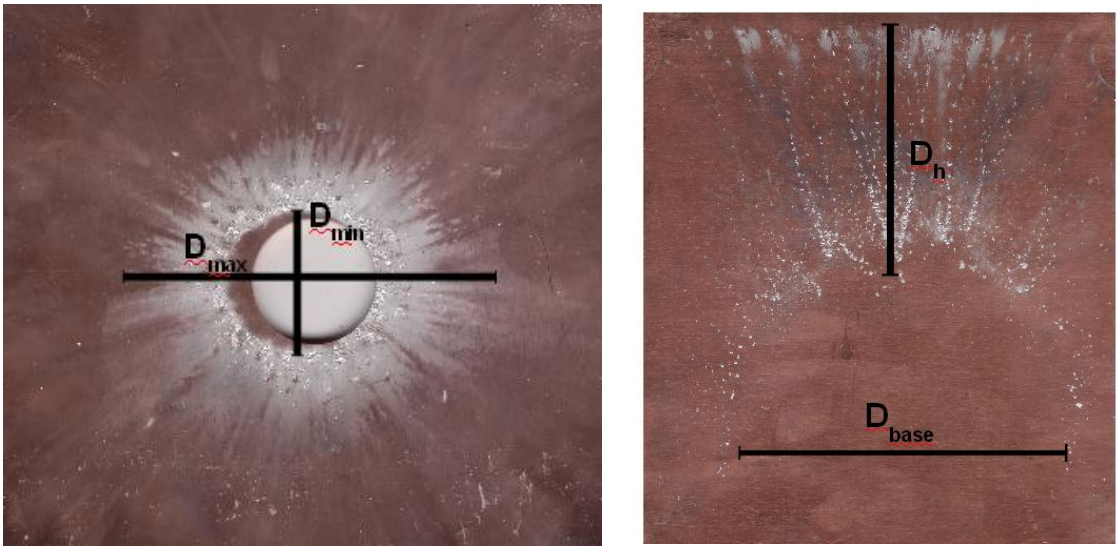

Fig. 2-5. Ejecta cloud footprint on witness plates: geometrical parameters for comparing experimental and numerical results regarding normal (left) and oblique (right) impacts

Test no.8648	D_{min} *(mm)*	D_{max} *(mm)*	$D_{average}$ *(mm)*
Experiment	22.4	60.7	41.5
Simulation	34.6	67.8	51.2

Tab. 2-6. ASI-CISAS test no.8648: comparison between experimental results and numerical simulation.

Test no.8657	D_{base} *(mm)*	D_h *(mm)*
Experiment	90.9	64.9
SPH	75.1	54.6

Tab. 2-7. ASI-CISAS test no.8657: comparison between experimental results and numerical simulation. The simulation was stopped when the ejecta cloud was still evolving

In both cases, a satisfactory agreement is reported between experimental results (in terms of witness plate global damage shape and extension) and numerical simulations.

2.4 ONERA synthesis model

This section describes the ejecta model developed by Onera (Mandeville and Rival, 1996) and later implemented in the ESABASE2/DEBRIS analysis tool.

The same model has been used for the computation of the contribution of ejecta particles to the population of small orbital debris. Approach is described in detail within the Final Report of the ISTC Project 3412 “Investigation of astrosols in the near earth space”. (Shutov and Zheltov, 2010)

The model is based upon a synthesis of available experimental data and theoretical/numerical results on ejecta phenomena.

Starting from knowledge of target (density ρ_t and brittle/ductile behavior), projectile (density ρ_p and mass m_p) and impact characteristics (velocity v_p and direction, given in terms of zenith θ and azimuth φ angles), the model computes the number of fragments having size between δ and $\delta+d\delta$,ejected with a velocity between v and $v+dv$ in the solid angle $d\Omega = \sin\theta \cdot d\theta \cdot d\varphi$ around the (θ, φ) direction:

$$n(\delta, \theta, \varphi, v) \cdot d\delta \cdot d\Omega \cdot dv \qquad \text{Eq. 2-6}$$

The frame is referenced to the satellite: the target (satellite surface) is fixed and velocities are relative to the target. Assuming a given impact site (point O) and a plane surface in the vicinity of impact point, The (x, y, z) coordinates frame is centered in O, with the z axis being perpendicular to the target surface. Spherical coordinates are used as well in the form (v, θ, φ).

It is assumed that the value of n in Eq. 2-6 is given by the sum of jet, cone and spall contributions for brittle targets and jet and cone particles only for ductile targets.

2.4.1 Total ejected mass

For estimating the total ejected mass, the basic equation by Gault (1973) is used as baseline together with a correction for application to ductile targets:

$$M_{e,tot} = \begin{cases} K \cdot 7.41 \cdot 10^{-6} \left(\dfrac{\rho_p}{\rho_t} \right)^{0.5} E_k^{1.133} \cos^2 \theta & \theta \le 60^\circ \\ K \cdot 3.71 \cdot 10^{-6} \left(\dfrac{\rho_p}{\rho_t} \right)^{0.5} E_k^{1.133} & \theta > 60^\circ \end{cases} \qquad \text{Eq. 2-7}$$

In the above equation, the $K=1$ for brittle targets and $K=0.001-0.01$ for ductile targets. Units

are SI.

2.4.2 Mass partitioning

The total ejecta mass is partitioned in three components as in Eq. 2-2. However, jetting is neglected by this model because there is a general consensus on the fact that the mass emitted within the jet is very low compared to that of cone and spall fragments. It should nevertheless be considered that the high velocity of jet particles could lead to significant secondary damage on components adjacent to the primary impact point.

With this assumption, Eq. 2-2 becomes:

$$M_{e,tot} \cong M_{cone} + M_{spall} \qquad \text{Eq. 2-8}$$

Specific models are then provided for the cone and spall mass:

$$M_{cone} = \beta \cdot M_{e,tot}$$
$$M_{spall} = (1-\beta) \cdot M_{e,tot} \qquad \text{Eq. 2-9}$$

Empirical equations are given in Tab. 2-8 for estimating the value of β in Eq. 2-9.

Target type	$d_p \leq 1\mu m$	$1\mu m < d_p \leq 10\mu m$	$10\mu m < d_p < 100\mu m$	$d_p \geq 100\mu m$
Ductile, homogeneous	$\beta = 1$	$\beta = 1$	$\beta = 1.$	$\beta = 1$
Brittle, homogeneous	$\beta = 1.$	$\beta = -0.3 \log d_p - 0.8$	$\beta = -0.3 \log d_p - 0.8$	$\beta = 0.4$
Brittle, solar cell	$\beta = 1.$	$\beta = -0.3 \log d_p - 0.8$	$\beta = -0.6 \log d_p - 2.3$	$\beta = 0.1$

Tab. 2-8. Values of β (Eq. 2-9) for different classes of targets and different projectile diameters (d_p unit is m)

2.4.3 Cone fragments modeling

Referring to cone fragments, the distribution of Eq. 2-6 is modeled in the following way:

$$n_{cone}(\delta,\theta,\varphi,v) = K_{cone}\, f_{cone}(\delta)\, g_{cone}(\theta)\, h_{cone}(\varphi)\, \Delta[v - v_{cone}(\delta,\theta,\varphi)] \qquad \text{Eq. 2-10}$$

In the above equation, Δ is the Dirac delta function and f_{cone}, g_{cone}, h_{cone} are probability density functions for fragments size, zenith and azimuth angles; v_{cone} is the velocity of the cone ejecta.

a. Size probability density

$$f_{cone}(\delta)=\frac{\alpha+1}{\delta_{\max}^{\alpha+1}-\delta_{\min}^{\alpha+1}}\delta^{\alpha}\,1_{[\delta_{\min},\delta_{\max}]} \qquad \text{Eq. 2-11}$$

In the above equation, 1 is the interval function, whose value is 1 if δ is within the [δ_{min}, δ_{max}] range and 0 elsewhere (δ unit is m); α is coefficient depending on the brittle or ductile behavior of the target, δ_{min} and δ_{max} are the minimum (cutoff) and maximum size of cone fragments:

Target type	α	δ_{min}	δ_{max}	λ ($\theta \leq 60°$)	λ ($\theta > 60°$)
Ductile	-2.6	0.1 μm	$\sqrt[3]{\frac{6\lambda M_{e,tot}}{\pi\rho_t}}$	0.01	0.05
Brittle	-3.5			0.1	0.5

Tab. 2-9. Values of coefficients in Eq. 2-11.

b. Zenith probability density

$$g_{cone}(\theta)=\frac{1}{\sigma\sqrt{2\pi}}\exp\left[-\frac{(\theta-\theta_{\max})^2}{2\sigma^2}\right]1_{[0,2\pi]} \qquad \text{Eq. 2-12}$$

In the above equation, angles are in radians and the suggested value for σ is 0.05 (i.e. ~3°). θ_{max} is the half aperture of the cone and depends on the projectile zenith angle θ_p, and the cone aperture for normal impact $\theta_{max,0}$ and oblique impact at ricochet limit $\theta_{max,60}$:

$$\theta_{\max}=\begin{cases}\dfrac{\theta_{\max,60}-\theta_{\max,0}}{\pi/3}\theta_p+\theta_{\max,0} & \theta\leq 60°\\ \theta_{\max,60} & \theta>60°\end{cases} \qquad \text{Eq. 2-13}$$

Suggested values for $\theta_{max,0}$ and $\theta_{max,60}$ are π/6 and 4π/9, respectively (these values seem to adapt to many cases involving different materials).

c. Azimuth probability density

$$h_{cone}(\varphi)=\begin{cases}\dfrac{1}{2\pi}\left[\dfrac{3\theta_p}{2\pi-3\theta_p}\cos(\varphi-\varphi_p)+1\right]1_{[0,2\pi]} & \theta_p\leq 60°\\ \dfrac{1}{\sigma'\sqrt{2\pi}}\exp\left[-\dfrac{(\varphi-\varphi_p)^2}{2\sigma'^2}\right]1_{[0,2\pi]} & \theta_p>60°\end{cases} \qquad \text{Eq. 2-14}$$

In the above equation, angles are in radians and the suggested value for σ' is 0.09 (i.e. ~5°).

It is evident that the density h_{cone} is uniform for normal impact. For oblique impact, h_{cone} is maximum for $\varphi=\varphi_p$ (downstream impact direction) and minimum for $\varphi=\varphi_p+\pi$ (backstream direction). The ratio between downstream and backstream densities is measured by the coefficient in front of the cosine. This ratio is equal to 1 for a normal impact; it increases with θ_p and becomes infinite for θ_p = 60° when the amount of fragments ejected in the backstream direction becomes zero.

d. Velocity probability density

It is assumed no dependence from the zenith angle:

$$v(\delta,\theta,\varphi)=\frac{v_{\max}(\varphi)-v_{\min}}{\delta_{\max}-\delta_{\min}}\cdot\frac{\delta_{\max}\delta_{\min}}{\delta}+\frac{v_{\min}\delta_{\max}-v_{\max}(\varphi)\delta_{\min}}{\delta_{\max}-\delta_{\min}} \qquad \text{Eq. 2-15}$$

Where v_{min}=10-100 m/s and:

$$v_{\max}(\varphi)=\begin{cases} v_p\cdot\left(1+\dfrac{6\theta_p}{\pi}\right)\cdot\left[\dfrac{3\theta_p}{4\pi}\cos(\varphi-\varphi_p)+1-\dfrac{3\theta_p}{4\pi}\right] & \theta_p\le 60° \\ 3v_p & \theta_p>60° \end{cases} \qquad \text{Eq. 2-16}$$

e. Normalization

The value of K_{cone} in Eq. 2-10 is found by integrating the n_{cone} distribution and imposing that the result equals the value of M_{cone} predicted by Eq. 2-9:

$$K_{cone}=\frac{6M_{cone}}{\pi\rho_t\sin\theta_{\max}}\cdot\frac{4-\alpha}{1-\alpha}\cdot\frac{\delta_{\max}^{1-\alpha}-\delta_{\min}^{1-\alpha}}{\delta_{\max}^{4-\alpha}-\delta_{\min}^{4-\alpha}} \qquad \text{Eq. 2-17}$$

2.4.4 Spall fragments modelling

As regards spall fragments, the distribution of Eq. 2-6 is modeled in the following way:

$$n_{spall}(\delta,\theta,\varphi,v)=K_{spall}\,f_{spall}(\delta)\,g_{spall}(\theta)\,h_{spall}(\varphi)\,j_{spall}(v) \qquad \text{Eq. 2-18}$$

In the above equation, f_{spall}, g_{spall}, h_{spall} and j_{spall} are probability density functions for fragments size, zenith and azimuth angles, and velocity.

a. Size probability density

$$f_{spall}(\delta) = \Delta(\delta - \delta_{spall})$$

$$\delta_{spall} = \sqrt[3]{\frac{6M_{spall}}{N_{spall}\pi\rho_t}} \qquad [m] \qquad \text{Eq. 2-19}$$

Eq. 2-19 assumes that M_{spall} (Eq. 2-9) is distributed between N_{spall} fragments having the same mass and equivalent diameter equal to δ_{spall}. It is suggested to adopt N_{spall} =10. Δ is the Dirac delta function.

b. Zenith probability density

$$g_{spall}(\theta) = \frac{1}{\theta_{spall}} 1_{[0,\theta_{spall}]} \qquad \text{Eq. 2-20}$$

In the above equation, it is assumed that θ_{spall}=0.09 (i.e. ~5°)

c. Azimuth probability density

$$h_{spall}(\varphi) = \frac{1}{2\pi} 1_{[0,2\pi]} \qquad \text{Eq. 2-21}$$

d. Velocity probability density

$$j_{spall}(v) = \Delta(v - v_{spall})$$

$$v_{spall} = 10 \div 100 \; ms^{-1} \qquad \text{Eq. 2-22}$$

e. Normalization

The value of K_{spall} in Eq. 2-18 is found by integrating the n_{spall} distribution and imposing that the result equals the value of M_{spall} predicted by Eq. 2-9:

$$K_{spall} = N_{spall} \cdot \frac{\theta_{spall}}{1 - \cos\theta_{spall}} \qquad \text{Eq. 2-23}$$

3 Experimental activity by WG3 member agencies

This section reports relevant experimental activity carried out by WG3 members on ejecta, with special attention to what has been recently done in the framework of the IADC AI 26-1 “Characterization of ejecta from HVI on spacecraft outer surfaces”.

3.1 ASI

Twenty-eight hypervelocity impact experiments [Francesconi et al, 2010] were carried out at CISAS-University of Padova impact facility in the framework of the ASI “Space Debris Program”, with the aim of contributing to IADC AI26-1 activities.
The objective was to count the number and to assess the size and speed distribution of ejecta from three different targets representative of spacecraft materials, i.e. simple aluminum-alloy plates, silicon solar cells and simple aluminum-alloy plates covered by MLI blankets. Projectiles having different size (1, 1.5 and 2.3 mm diameter) were launched at speed ranging from 4 to 5.5 km/s and impact angle from 0° to 80°. Laboratory instrumentation and analysis methods to characterize ejecta produced during LGG impact testing were developed as well.

3.1.1 Experimental setup

The instrument package for ejecta characterization was conceived to satisfy the two following requirements:

- To count the number and measure the equivalent diameter of craters left on witness plates located close to the target in order to record the footprint of the ejecta cloud;
- To infer information about the size-speed distribution of the ejecta fragments that have produced the crater patterns earlier analyzed on witness plates.

According to the above requirements, a simple system to mount the experiment into the LGG impact chamber was realized (Fig. 3-1), consisting in two independent supporting frames on which the target and the copper witness plates are fixed. The choice of having two separate supports makes possible to easily change their mutual orientation and hence the impact angle.

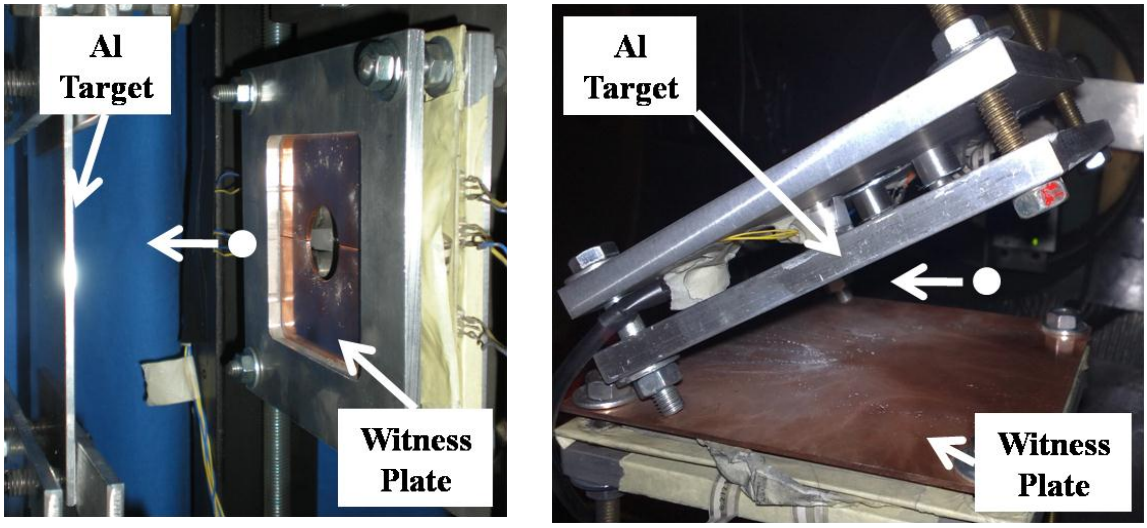

Fig. 3-1. Instrument for ejecta characterization: normal (left) and oblique (right) impact configuration. In the normal impact configuration, a central hole is evident in the witness plate to allow the projectile pass through the plate and reach the target.

The witness plate is connected to the frame structure through six sensorized pins on which strain gauges are bonded to record the propagation of pressure waves generated by the ejecta cloud impact onto the plate itself (Fig. 3-2).

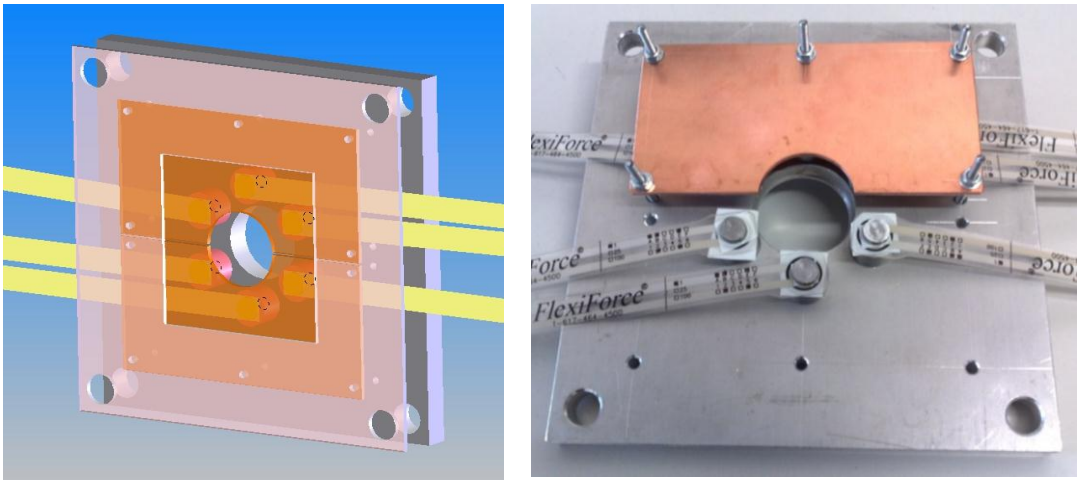

Fig. 3-2. Copper witness plate supported on sensorized pins

Thanks to an appropriate time reference given by an impact flash detector that is sensitive to the light emitted by the projectile hitting the target, strain gauges signals can provide a time-of-flight information for the ejecta cloud tip and hence a redundant assessment of the speed of the fastest ejecta particle. In some situation, even the impact flash detector can be used directly to assess the bulk velocity of the ejecta cloud, since both the target and the witness plate are contained in its field of view and it can therefore record two separate flashes, one originated from the primary impact and the other produced by the secondary one.

3.1.2 Test summary

Tab. 3-1 below provides a summary of the experiments conducted within the test program. In every test, pure copper witness plates 2 mm thick were employed.

Test ID	*Target material*	*Target thickness (mm)*	d_p *(mm)*	v_p^* *(km/s)*	α *(°)*
8621	Al7075-T6	3	1.0	5.03	0
8622	Al7075-T6	3	2.3	5.29	0
8629	Al7075-T6	3	1.5	4.71	0
8630	Al7075-T6	3	1.5	4.41	0
8631	Al7075-T6	3	1.0	4.47	0
8632	Al7075-T6	3	2.3	4.40	0
8646	Al7075-T6	10	1.5	5.20	0
8647	Al7075-T6	10	1.5	4.22	0
8648	Al7075-T6	10	2.3	5.34	0
8649	Al7075-T6	10	2.3	4.47	0
8650	Al7075-T6	10	1.0	4.42	0
8655	Al7075-T6	10	1.0	5.10	45
8656	Al7075-T6	10	2.3	5.34	45
8657	Al7075-T6	10	2.3	5.29	60
8658	Al7075-T6	10	1.0	5.29	60
8659	Al7075-T6	10	1.5	5.23	60
8660	Al7075-T6	10	1.5	5.25	45
8662	Al7075-T6	10	1.5	5.16	80
8664	Al7075-T6	10	2.3	5.29	80
8623	Al7075-T6 + MLI	3	2.3	5.29	0
8634	Al7075-T6 + MLI	3	1.5	5.36	0
8635	Al7075-T6 + MLI	3	1.5	4.39	0
8637	Al7075-T6 + MLI	3	1.0	4.35	0
8638	Al7075-T6 + MLI	3	2.3	4.46	0
8626	Si Solar cell	3**	1.0	4.97	0
8627	Si Solar cel	3**	2.3	5.16	0
8640	Si Solar cell	3**	1.0	4.20	0
8641	Si Solar cell	3**	2.3	4.23	0

Tab. 3-1. ASI/CISAS test program for ejecta characterization: summary. d_p, v_p and α are respectively the projectile diameter, velocity and impact angle

* Uncertainty in speed measurement is always below or equal to 3%

** Cover glass thickness

3.1.3 Data utilization

For each experiment, the first information acquired includes the number and size of witness plate craters, obtained through the automatic analysis of high-resolution (1200 dpi) witness

plate photographs. However, this is not enough to derive size-speed probability functions for ejecta, since craters extension is not sufficient to univocally determine the velocity and size of the particles that caused the damage. A second piece of information is therefore given by the signals of the impact flash detector and the strain gauges bonded to witness plates, which provide an estimation of the ejecta cloud tip speed with its related uncertainty. The last input to the analysis procedure is provided by well-known empirical crater equations which correlate crater diameter and depth observed on witness plates to the size and speed of the ejecta particles that produced the damage. In the framework of this activity, Eq. 3-1 [Lambert, 1997] and Eq. 3-2 [Tanaka et al, 2008] were arbitrary selected: specific assessment of the adequateness of different crater equations was not performed, since the main focus was the methodology's development: once a suitable analysis procedure is outlined, other equations could be used in the same way, affecting only the overall method uncertainty.

$$p = k_{\infty} \rho_p^{1/6} m^{0.352} v_n^{2/3} \qquad \text{Eq. 3-1}$$

$$p / d_c = 9.60 \cdot \left(\frac{v_n}{c_T} \right)^{1.18} \qquad \text{Eq. 3-2}$$

In the previous equations, p and d_c are the crater depth and diameter expressed in cm; ρ_p, m and v_n are the impactor density, mass and normal speed expressed in gcm^{-3}, g and km/s; c_T is the speed of propagation of longitudinal waves in the target expressed in km/s and k_∞ is a constant depending from the target material's hardness (k_∞ was assumed to vary in the range 0.40-0.45 for copper).

A flow chart of the procedure for data analysis is presented in Fig. 3-3.

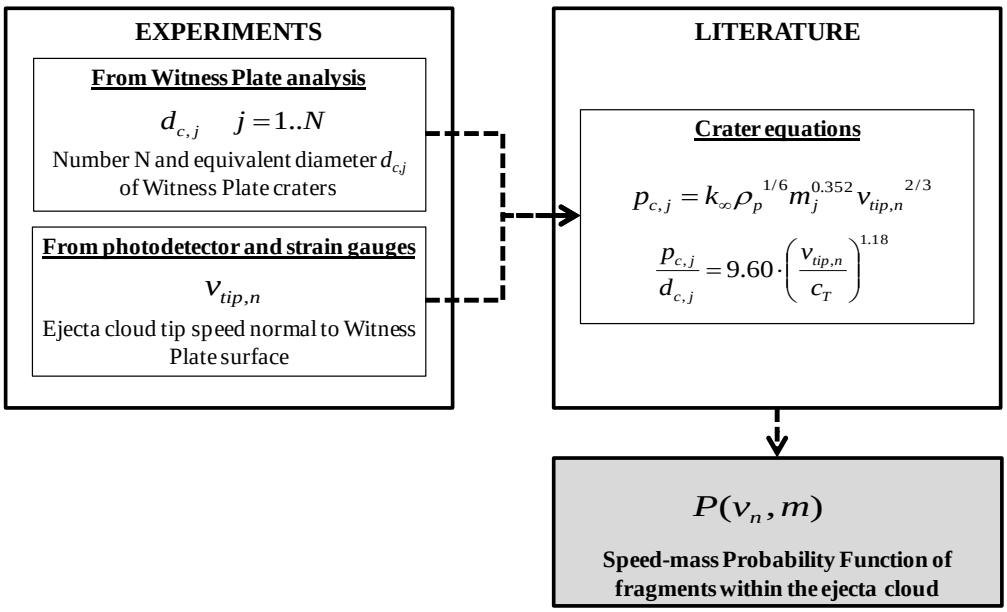

Fig. 3-3. ASI/CISAS data analysis procedure

Experimental results (craters number and size, ejecta velocity distribution) are used as input to available crater equations, to finally obtain mass-speed probability functions which describe the

characteristics of fragments within each ejecta cloud.
Some further details on the analysis steps presented in Fig. 3-3 are given in the remainder of this section.

a. Witness plates analysis

High-resolution images of copper witness plates were analyzed to infer information about craters pattern, distribution and size. For this purpose, specific ad-hoc software was developed in Matlab environment. Craters identification, counting and measurement are based upon the identification of color variations in pictures properly treated through the application of specific color maps. Moreover, to avoid erroneous craters identifications due to scratches or imperfections of the plate, comparisons were implemented between images of the plates before and after the experiment: damage features recognized on both pictures are labeled as “false positives” and then cancelled from the analysis results. Accepted craters are finally sorted in four bins referring to the following ranges of equivalent diameter: 0.025 to 0.05 mm, 0.05 to 0.1 mm, 0.1 to 1 mm and >1mm. Final and intermediate analysis results are made available in both graphical and in data structure format while a text report is provided with all the analysis messages.
Two examples of the witness plate analysis procedure are given in Fig. 3-4 and Fig. 3-5, referring to shots no. 8646 and 8656 respectively (see Tab. 3-1 to review the relevant test parameters). In both figures, left pictures are raw images of the witness plates after the test and right pictures highlight the “real” craters identified after “false positives” deletion. In the central pictures, green and blue symbols highlight damage features recognized on pre-shot (e.g. due to plate imperfections) and post-shot images, respectively; magenta and cyan symbols are features that are present on both pre-shot and post-shot pictures and are therefore labeled as “false positives”; red squares mark craters that come out from the post-shot image only and hence they are recognized as “real craters”.

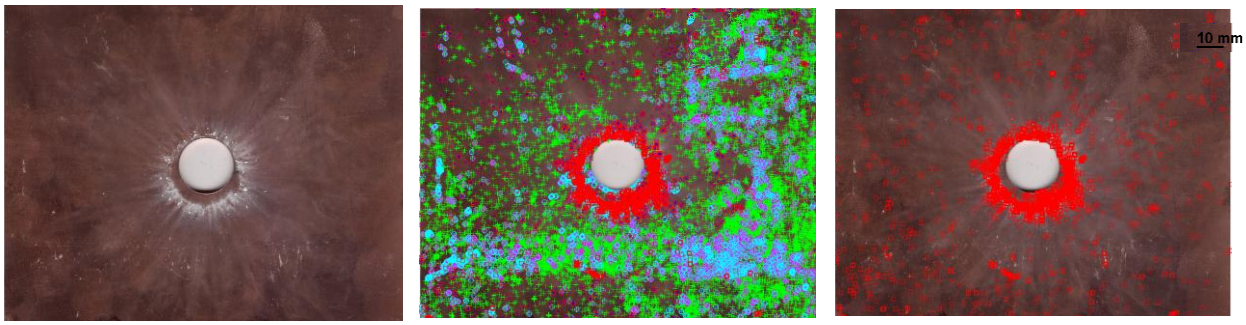

Fig. 3-4. ASI/CISAS impact tests. Witness plate analysis for shot no. 8646 (1.5 mm projectile at 5.20 km/s on a 10 mm Al6082-T6 plate, normal impact): raw image (left), damage features recognized by the analysis (center), craters identified after “false positives” subtraction (right).

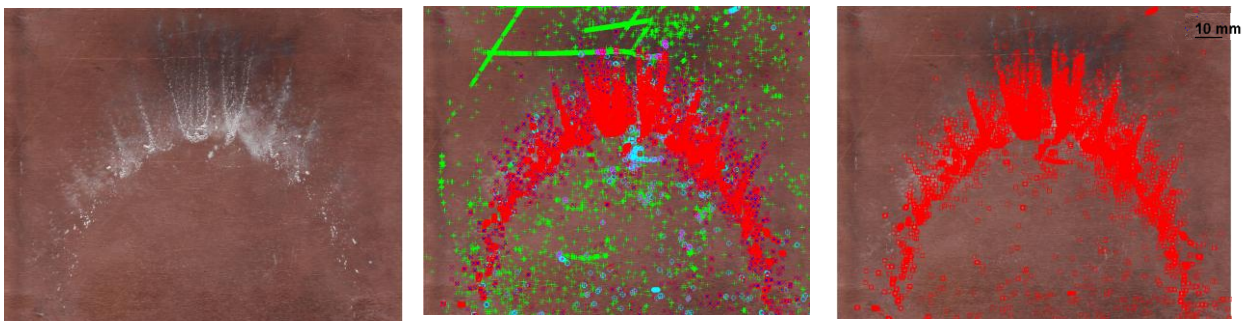

Fig. 3-5. ASI/CISAS impact tests. Witness plate analysis for shot no. 8656 (2.3 mm projectile at 5.34 km/s on a 10 mm Al6082-T6 plate, 45° impact): raw image (left), damage features recognized by the analysis (center), craters identified after "false positives" subtraction (right).

b. Time-of-Flight measurements

Among the complexity of the instrumentation, to estimate the ejecta speed is indeed much more critical than measuring the craters extent on witness plates. In fact, ejecta clouds are complex structures in which particles of various size travel in different directions and have a wide range of velocities. In this framework, only the ejecta cloud tip speed was estimated, which indeed could give a misleading picture of the phenomenon under investigation.

An impact flash photo-detector and six strain gauges on the witness plates supports were used to provide an estimation of the time of flight of the ejecta cloud travelling from the target to the witness plate. In fact, the photo-detector is sensitive to the light emitted by the primary impact onto the target and the secondary impact onto the plate, while the strain gauges record the stress waves propagating along the witness plates as a consequence of the transient load imparted by the cloud to the structure. Sample signals of the photo-detector and one strain gauge are presented in Fig. 3-6. All of them were sampled at 1 MS/s and therefore provide enough time resolution for the Time-of-Flight (ToF) estimation.

It appears that the photo-detector records the flash emitted by both the primary and secondary impact: the projectile hitting the target produces a narrow signal, while the ejecta cloud provides a wider signal, since its impact on the witness plate is much more distributed in time according to the fragments speed range. In conclusion, taking the narrow peak maximum as reference (t_0 defines the instant on which the primary impact occurs), the average and standard deviation of the debris cloud time of flight can be estimated through the identification of t_1 and t_2 (we assumed a Gaussian distribution for the ejecta cloud speed, although different assumptions might be considered to better represent the velocity scatter within the cloud):

$$ToF_{avg} = t_2 - t_0$$
$$\sigma_{ToF} = t_2 - t_1 \qquad \text{Eq. 3-3}$$

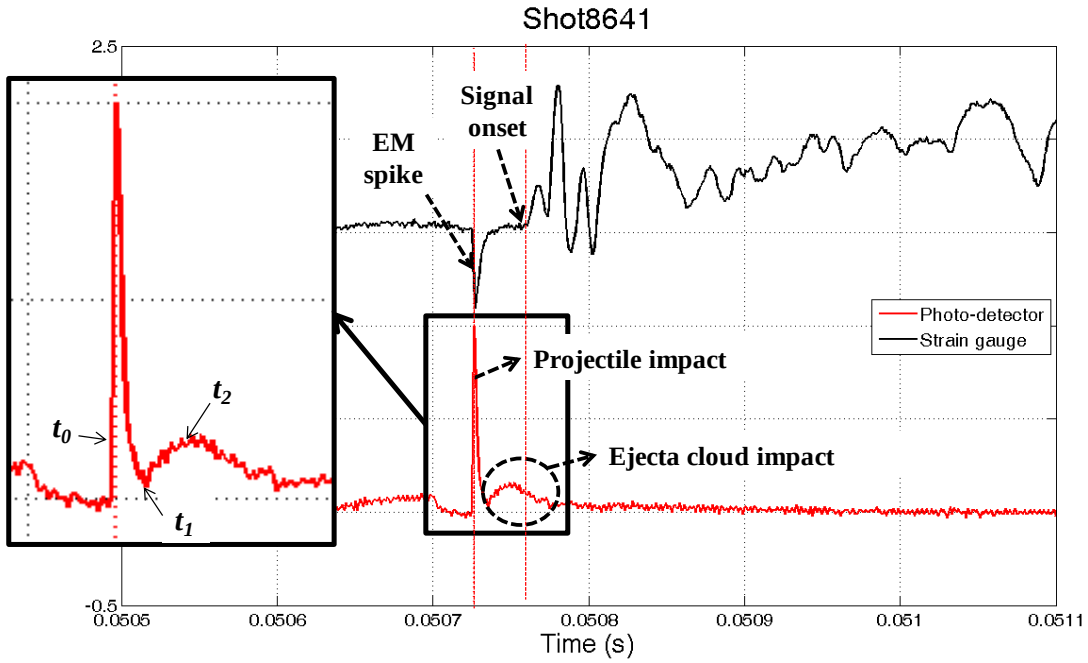

Fig. 3-6. ASI/CISAS impact tests. Shot no. 8641. Impact flash detector (red) and strain gauge (black) signals

Considering the strain gauge, two signal features are evident in Fig. 3-6. Referring to the debris cloud impact, a certain delay appears between the onsets of the photo-detector and strain gauge signals. This is due to the finite time of propagation of stress waves in the witness plate material between the impact zone and the sensor and introduces a systematic error in the ToF estimation that can be corrected with some effort. Another drawback in using the strain gauge is that it records the dynamic response of the plate and it can provide only the time of arrival of the wave to the sensor, since further oscillations continue until the plate vibration modes are damped, even if the impact phenomenon is over. For these reasons, the use of the photo-detector should be preferred for ToF estimation, as far its output has adequate signal to noise ratio. In fact, there are materials which do not emit enough light upon impact (e.g. MLI, Kevlar, Nextel, etc.) and in such cases the employment of information coming from strain gauges becomes unavoidable.

Once the ToF is assessed, the ejecta speed v_n along a direction perpendicular to the witness plate is simply computed dividing the normal distance between the target and the witness plate by the time of flight. The standard deviation σ_{vn} is obtained accordingly.

3.1.4 Results

Results about craters counting and craters size estimation are presented hereafter. Even though craters counting does not provide information about the mass and speed of fragments which produce the damage, it nevertheless gives a first idea of the extent of the ejecta phenomenon, offering also the opportunity of comparing the behavior of different spacecraft materials in various impact conditions.

Three figures are presented in the following, each of them referring to experiments performed using projectiles having fixed size (d_p= 1mm in Fig. 3-7, d_p=1.5 mm in Fig. 3-8 and d_p=2.3 mm in Fig. 3-9). In the three cases, the number of craters is plotted as a function of the impact velocity range (two speed bins have been considered: 4.0-4.5 km/s and 5.0-5.5 km/s) and the crater diameter range (four size bins have been considered: 0.025-0.05 mm, 0.05-0.1 mm, 0.1-1 mm and >1 mm). The images on the left compare the behavior of different target materials and configurations, while the images on the right evaluate the response of a single target configuration (Al 6082-T6 alloy, 10 mm thick) with different values of the impact angle.

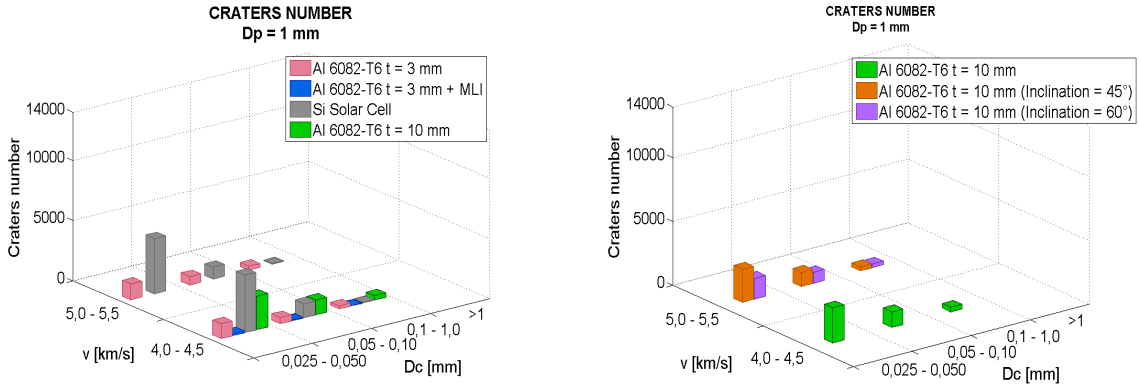

Fig. 3-7. ASI/CISAS impact tests. Number of craters for d_p=1 mm.

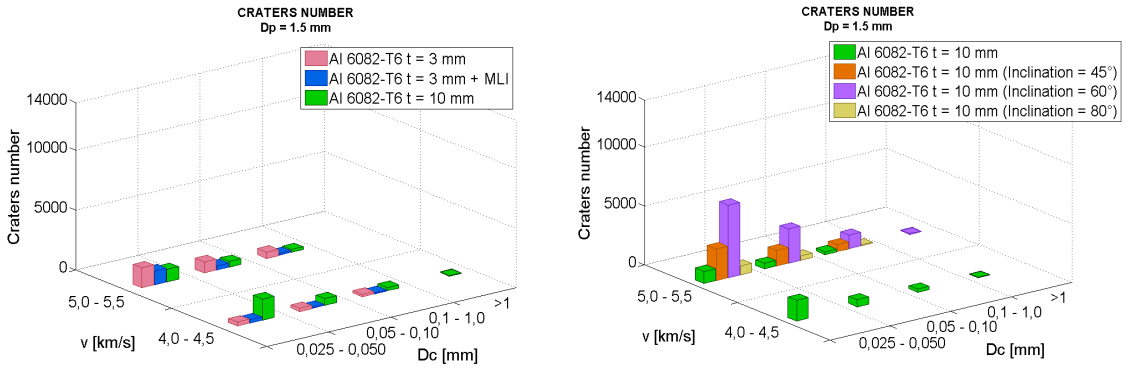

Fig. 3-8. ASI/CISAS impact tests. Number of craters for d_p=1.5 mm.

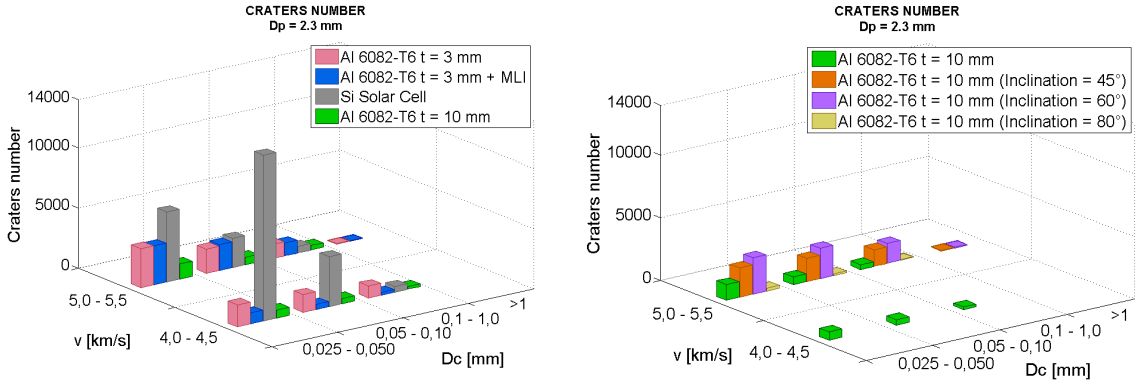

Fig. 3-9. ASI/CISAS impact tests. Number of craters for d_p=2.3 mm.

Even considering the scattering of results, some important conclusion can be immediately drawn by looking at the three above figures:

- A single HVI on whatever spacecraft material produces a significantly high number of new debris (order of thousands) in a wide size range up to the magnitude of the original one;
- HVI with large debris create more ejecta than impacts with small ones and increasing the impact velocity causes a slight raise of the fragments number;
- HVI on brittle materials (e.g. solar cells cover-glass) produce more ejecta than impacts on ductile ones (e.g. metals), but the environment pollution and the damage potential of particles coming from metals are higher, since large fragments seem to be prevalent; moreover, metals covered by MLI blankets generate less fragments than similar targets without MLI;
- The impact obliquity seems to have a non-monotonous effect: the number of ejecta increase from 0° to 45°, then is almost stable up to 60° and finally falls down significantly above 60°.

3.2 CNES

An impact test was performed at Centre d'Etudes de Gramat (CEG, France) with a light-gas gun able to accelerate millimetre-sized projectiles to hypervelocity, with a limit of 10 g launch package launched at 8 km/s [Loupias, 1996].

After the shot of a 5 mm steel projectile at 5.6 ± 0.2 km/s on an Al6061-T6 target 35 mm thick, ejecta were collected on a copper witness plate 1 mm thick, located at 148 mm in front of the target. The number of secondary impacts (due to cone ejecta) on the witness plate was lower than that obtainable from brittle targets, there were no spall fragments and the total ejected mass was rather low. The primary crater volume was about 1 cm^3, corresponding to about 3g of aluminium. However, it should be considered that a significant part of material was compressed at the bottom of the crater, or remained attached to the target by forming a lip around the crater.

The witness plate is shown in Fig. 3-10, left. The location of secondary impacts on a ring gives an evidence for the conical shape of the ejecta cloud; cone angle is about 34°, which corresponds to a 56° elevation angle; width of the ring on the witness plate corresponds to an angle of about 6°. The number of secondary craters is maximum at the centre of the ring, and decreases at the periphery. The size distribution is homogeneous on the whole ring. The cumulative size distribution of craters larger than 100μm (referring to three positions near the ring centre) is shown in Fig. 3-10, right. The slope of the distribution is about -1.6, that gives a -2.6 value for the α coefficient of the ejecta size distribution (see section 2.2.2). Depth to diameter ratio of secondary craters is close to 0.2: this value suggests that ejecta larger than 100μm have an ejection velocity less than 1km/s.

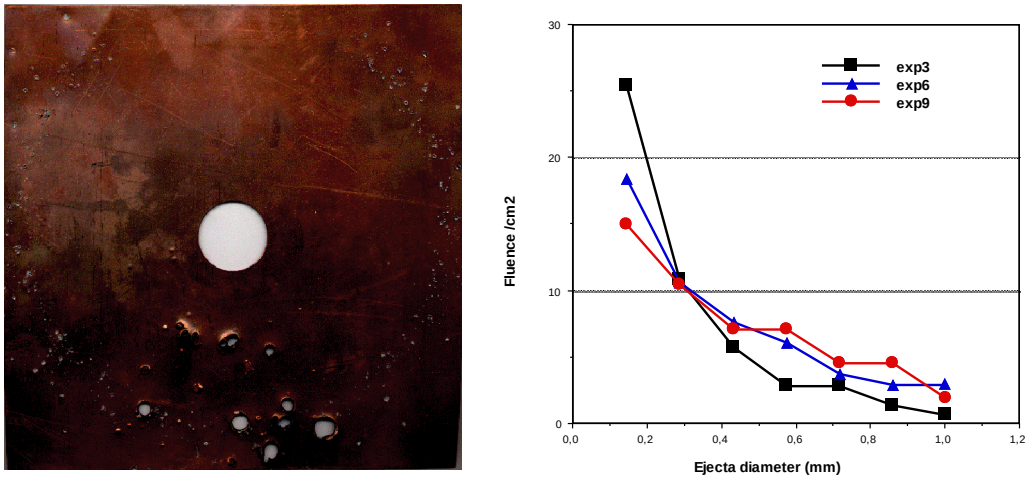

Fig. 3-10. Witness plate used in the CNES/CEG test (5mm AISI304 projectile impacting an Al6061-T6 35 mm thick plate at 5.6 km7s): ejecta damage (left) and cumulative size distribution of craters (right)

3.3 DLR

Experimental tests with light-gas gun were performed at EMI (Freiburg, Germany) on solar cell samples from the Hubble Space Telescope (HST) using ~500 μm glass bead projectiles at speed close to 5 km/s. Impact angle of 30°, 45° and 60° [Schaefer and Schneider, 1997]. Test conditions are presented in Tab. 3-2.

Test ID	*Target material*	d_p *(μm)*	v_p^* *(km/s)*	α *(°)*	*Comments*
2677	HST solar cell	500	4.5	30	Small secondary ejecta
2684	HST solar cell	500	4.8	45	Target perforation
2686	HST solar cell	500	4.8	60	Target perforation

Tab. 3-2. Test performed on Hubble Space Telescope (HST) solar cell samples at EMI (Germany): impact conditions

For tests performed with an incidence of 30° and 45°, the ejection angles corresponding to the maximum of ejecta were consistent with models predictions, the cone of ejecta was however widely open with a value of 15-20°. For test case 2686, with an incidence of 60°, the angular distribution was characterized by a narrow band, heavily cratered, however the limit for the ricochet was not reached (the difference with other experiments reported in the literature could be due to the use here, of glass material as projectile).

Test ID	*Ejecta cone angle Experiment (°)*	*Ejecta cone angle Model (°)*	*Comments*
2677	45	55	Spread: 15°
2684	62	67	Spread: 20°
2686	85	80	Spread: 4°

Tab. 3-3. Test performed on Hubble Space Telescope (HST) solar cell samples at EMI (Germany): ejecta cone angles

Microscopic observation of test sample 2684 (Fig. 3-11) provides interesting results about the size distribution and the amount of ejecta. The crater is typical of impact perforation produced on solar cells. The shape reflects the oblique incidence (45°). The mean diameter of the conchoidal zone is 2750 µm; the cover glass (thickness 150 µm) was crushed and ejected within two zones, i.e. a circular conic zone with an outer diameter of 2750 µm and an inner diameter of 1500 µm and a cylindrical central zone with a diameter of 1500 µm.

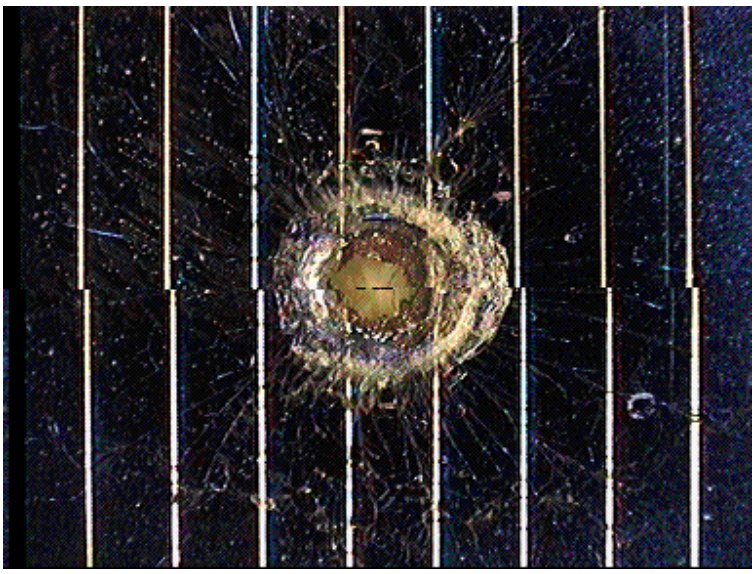

Fig. 3-11. EMI test no. 2684: HST solar cell sample hit by a 0.5 mm projectile at 4.8 km/s, 45° impact angle

The silicon layer (thickness 250 µm) was crushed and ejected within a central zone, 1500 µm in diameter. Taking into account these data it is possible to estimate the total mass of material ejected during the impact as M_{ej} = 2.43x10^{-3} g. Since the mass of a 500 µm glass projectile is m_p= 1.6x10^{-4} g, the ratio of the ejected mass to the mass of the impactor is $M_{ej}/m_p \cong 15$. Using the equation proposed by Gault [1973] for the computation of total mass ejected upon cratering of a simple semi-infinite brittle target gives a ratio of about 50. Considering that in our case the target (formed of several layers of materials bound by an adhesive) was perforated (with a significant ejection of matter downstream) the agreement between both results is reasonably good.

Many small fragments (some could have been trapped by the adhesive used for the manufacturing of the cells) are still visible inside the crater: their sizes vary from 5 µm (optical resolution limit) to 30 µm. The smallest are roughly cubical in shape, the largest are elongated fragments. Some large (100 µm) spall fragments in the outer spall zone were not ejected.

The cumulative number of craters split in different size bins are shown in Tab. 3-4.

Crater equivalent diameter (μm)	*No. of craters Test no.2684*	*No. of craters Test no.2686*
>500	0	8
200-500	0	65
100-200	0	140
50-100	180	350
20-50	400	0
10-20	3500	7500
5-10	0	26000

Tab. 3-4. Test performed on Hubble Space Telescope (HST) solar cell samples at EMI (Germany): cumulative number of craters per size

3.4 JAXA

Two main programs were recently conducted in Japan referring to ejecta characterization.
On one hand, a study was performed in collaboration with Kyushu Institute of Technology (KIT) in the framework of ISO activities for defining a standard test procedure to evaluate spacecraft ejecta upon hypervelocity impact [Sugahara et al, 2009]. Distribution of ejecta fragments was evaluated from craters on witness plates and the measurement process was suggested by JAXA as a method of facility calibration for ejecta tests.
On the other hand, the Nagoya Institute of Technology (NIT) investigated the difference of ejecta distributions according to projectile density and heat treatment of target materials [Nishida et al, 2010]. Craters in witness plates were analyzed with an X-ray spectrometer to evaluate the ejecta fragment cloud structure. Size distribution of ejecta particles was also obtained from fragments recovered in the test chamber.

3.4.1 Tests for evaluating standard procedures for ejecta characterization

HVI experiments were conducted with two-stage light gas guns at Kyushu Institute of Technology (KIT) and the Institute of Space and Astronautical Science/JAXA (ISAS). Their calibers are 5 and 7 mm, respectively. Post-impact analysis was conducted at KIT.

a. Impact conditions and experimental setup

Al2017 spheres (1 mm diameter) were used as projectiles and were accelerated to 4 and 5 km/s. In general, a large amount of spall fragments is generated from targets made by brittle materials (e.g. silica), and samples can be broken by the impact pressure. For these reasons, brittle targets were covered with a rubber sponge and an aluminum case (Fig. 4-1). Witness plates were mounted as shown in Fig. 3-12 (in case of thin targets, two witness plates were installed in front and behind the sample). Copper alloy (C1100P-1/4H) witness plates were mounted parallel to the target impact surface and the standoff distance was 100 mm. The front witness plate had a hole of 30 mm in diameter.

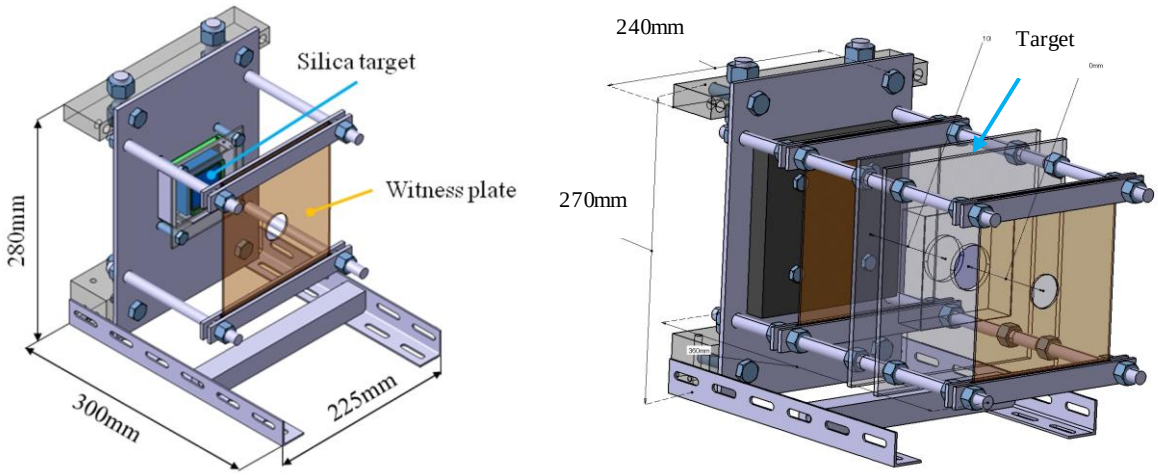

Fig. 3-12. JAXA/KIT impact tests. Experimental configurations for semi-infinite targets (left) and thin targets (right)

b. Post-impact analysis

The mass of the target was measured before and after the experiment to assess the total amount of ejecta fragments $M_{e,tot}$. The obtained values were compared to those predicted by Eq. 3-4 [Gault, 1973] to empirically calculate the value of K in the equation.

$$M_{e,tot} = K \times 7.41 \times 10^{-6} \left(\rho_p / \rho_t\right)^{0.5} E_i^{1.133} \left(\cos\theta_i\right)^2 \qquad \text{Eq. 3-4}$$

K is a material-dependant coefficient, ρ_p and ρ_t are the density of projectile and target, E_i is the projectile kinetic energy, and θ_i is the impact incidence angle.

Position and size of craters on the witness plates were measured with a microscope system (Fig. 3-13) having 0.025 mm resolution. Craters were detected by comparing witness plate images recorded before and after the impact test.

Craters shape was approximated by an ellipse, and the average of major and minor axes was defined as crater equivalent diameter.

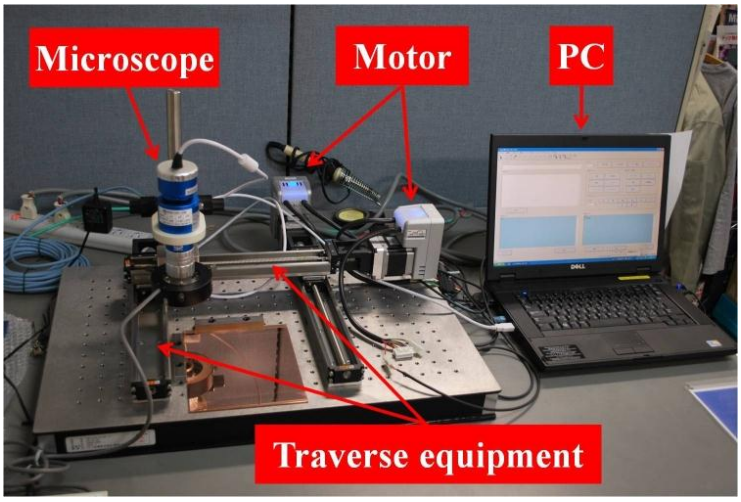

Fig. 3-13. Microscope system for witness plate craters analysis

In order to investigate the effect of witness plate surface roughness on the crater analysis procedure, 3 types of surface finishes were considered: un-processing, buffing and chemical polishing (Fig. 3-14).

Results are compared in Fig. 3-15: in the case of the unprocessed plate, it was difficult to distinguish craters smaller than 0.05 mm from features already present before the impact tests and the damage distribution was significantly different than those obtained in the other cases. Meanwhile, the results of buffing and chemical polishing were almost the same.

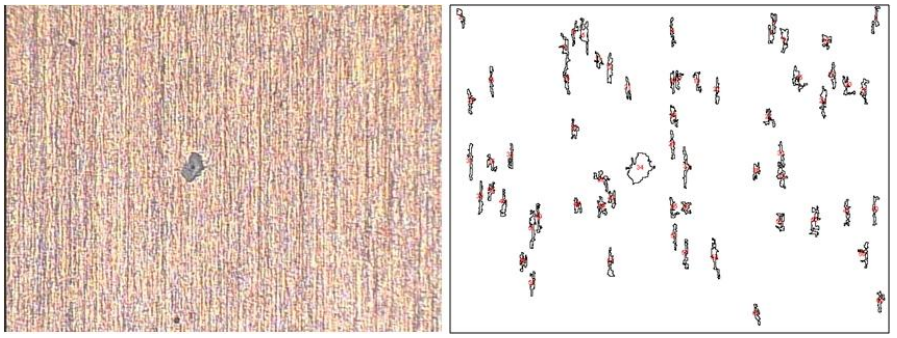

(a) unprocessed

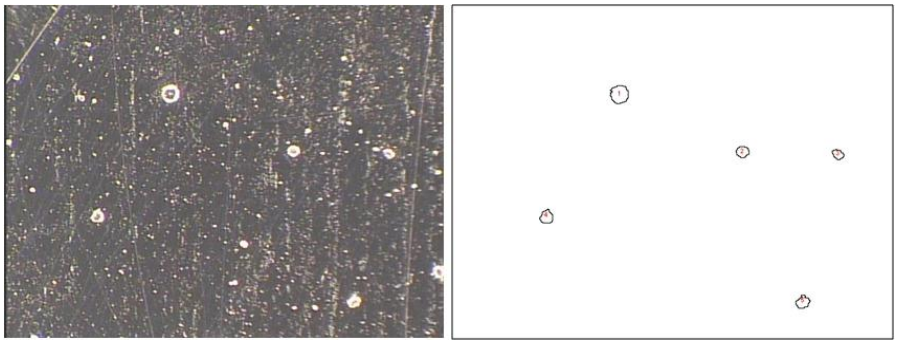

(b) buffing

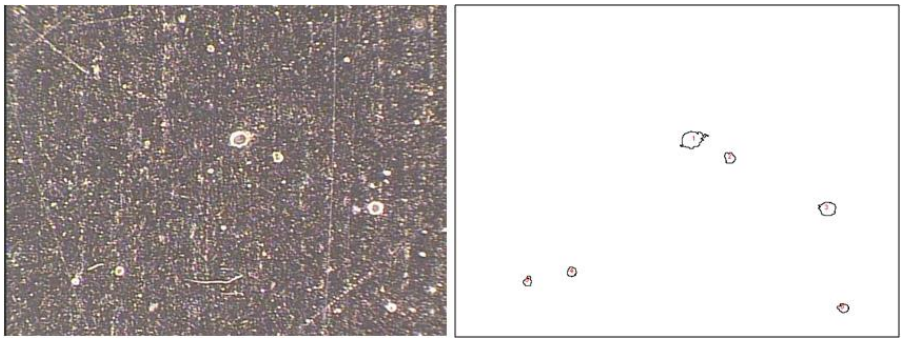

(c) chemical polishing

Fig. 3-14. JAXA/KIT impact tests. Automatic crater analysis on plates with different surface finishes: damage features detected

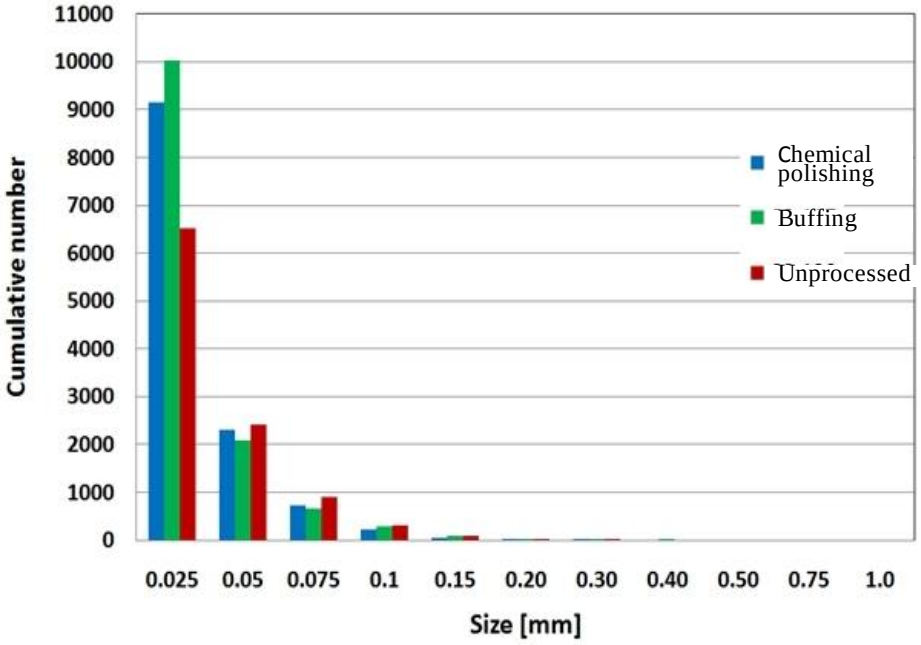

Fig. 3-15. JAXA/KIT impact tests. Automatic crater analysis on plates with different surface finishes: comparison of results

c. Results on SiO_2 targets

Craters counting and measurement was performed on a witness plate used for an impact test on a SiO_2 target (Fig. 4-1). Impact speed was 3.71 km/s. Ejecta mass was 70.2 mg. Size distribution of craters is shown in Fig. 3-16. Scatter angle of the ejecta fragments was 35°. Number and size of craters is shown in Tab. 3-5.

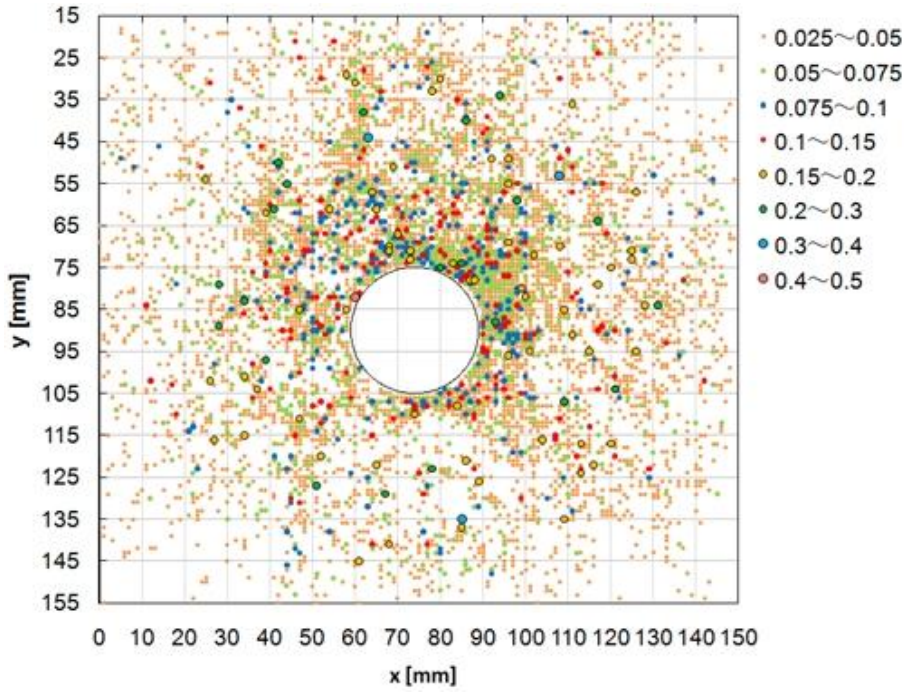

Fig. 3-16. JAXA/KIT impact test on SiO_2 target. Automatic crater analysis on plates with different surface finishes: comparison of results

Diameter range (mm)	*0.025 to 0.05*	*0.05 to 0.075*	*0.075 to 0.10*	*0.10 to 0.15*	*0.15 to 0.20*	*0.20 to 0.30*	*0.30 to 0.40*	*0.40 to 0.50*	*0.50 to 0.75*	*0.75 to 1.0*
Number of craters	7944	1420	376	196	64	21	3	1	0	0

Tab. 3-5. JAXA/KIT impact test on SiO_2 target. Number of craters

3.4.2 Effects of projectile density and target heat treatment on ejecta distributions

HVI experiments were conducted with two-stage light-gas guns at Nagoya Institute of Technology (NIT) and the Institute of Space and Astronautical Science/JAXA (ISAS). Their calibers are 14 and 7 mm, respectively. Post-impact analysis was conducted at NIT.

a. Impact conditions and experimental setup

Spherical projectiles (3.2, 7.1, and 14.3 mm) made by polycarbonate, steel, iron, and aluminum alloy were launched at 2, 4 and 6 km/s.
Copper alloy (C1100P-1/4H) witness plates were mounted in front of targets (Fig. 3-17) at a 50 mm standoff. Witness plate holes were 20 mm except for 3.2 mm projectiles (in this case, hole diameter was 30 mm). Targets were made of A1100-O, A1100-H, A6061-O, and A6061-T6 aluminum alloy.

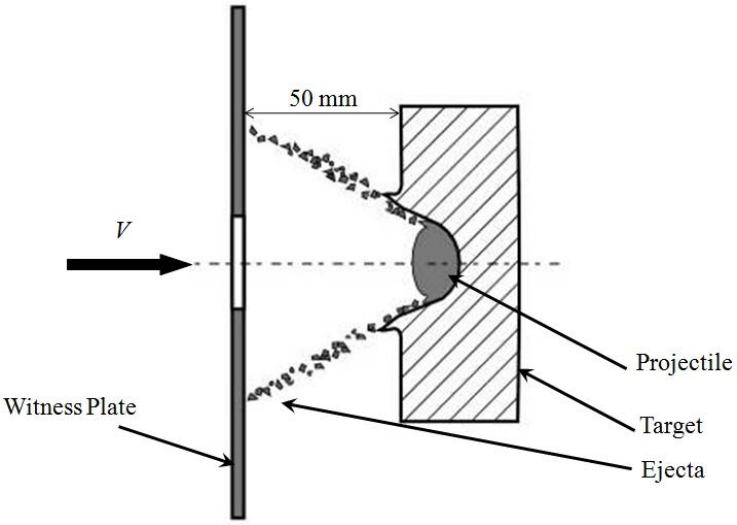

Fig. 3-17. JAXA/NIT test setup

b. Post-impact analysis and results

Front velocity of ejecta clouds was measured by images from a high speed camera. Ejecta fragments larger than 0.001 g were collected from the test chamber (Fig. 3-18, left) and their mass and size were measured, providing a fragment characteristic length $L_c = (a+b+c)/3$ (the

geometric model for size measurements is shown in Fig. 3-18, right). The ejecta cone angle was estimated starting from the crater distribution on witness plates (Fig. 3-19). Craters were analyzed with an energy dispersive X-ray spectrometer to identify the material of impacting fragments.

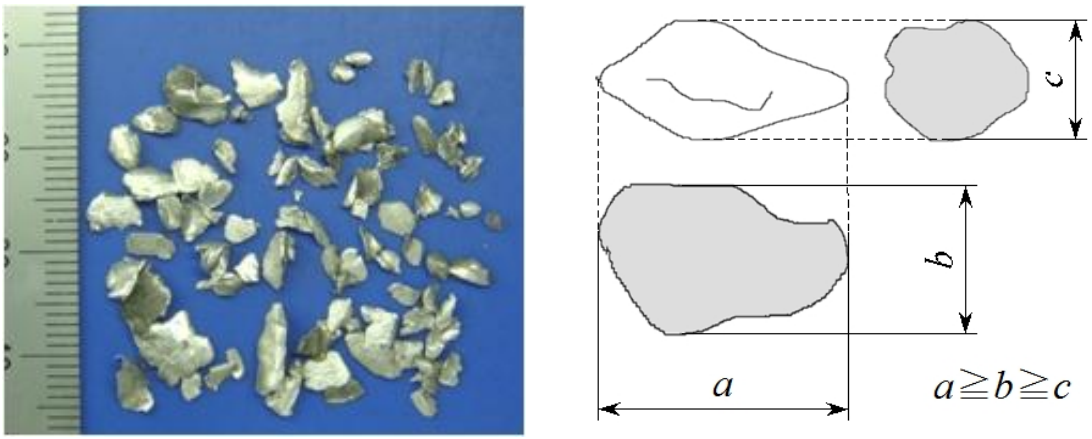

Fig. 3-18. JAXA/NIT impact tests. Ejecta fragment collected after an impact test (left). Fragment geometric model (right)

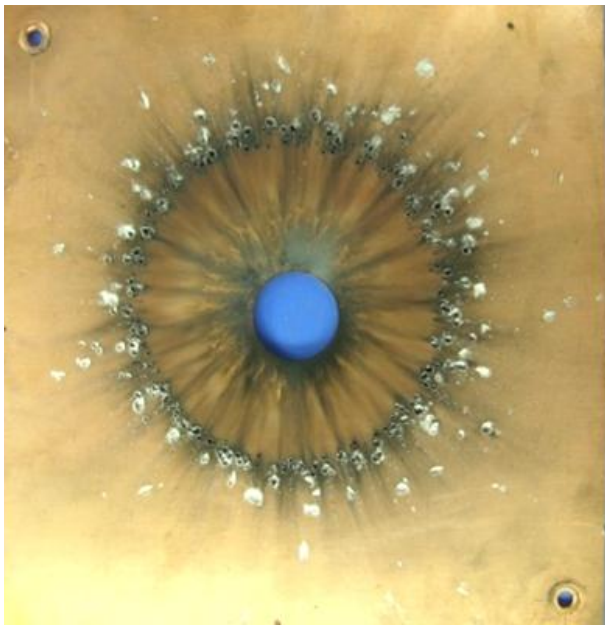

Fig. 3-19. JAXA/NIT impact tests. Witness plate used in an experiment on a A6061-T6 target

c. Results

In case of impacts at v_p=6 km/s of 7.1 mm polycarbonate projectiles, the front velocity of the ejecta cloud was in the range 0.8-1.2 v_p. The number and average cross section of collected ejecta fragments are shown in Fig. 3-20 and Fig. 3-21, respectively.

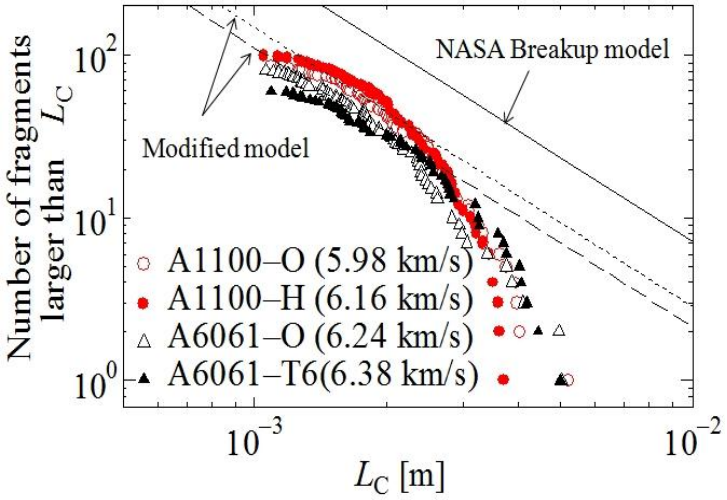

Fig. 3-20. JAXA/NIT impact tests. Cumulative number of collected ejecta fragments

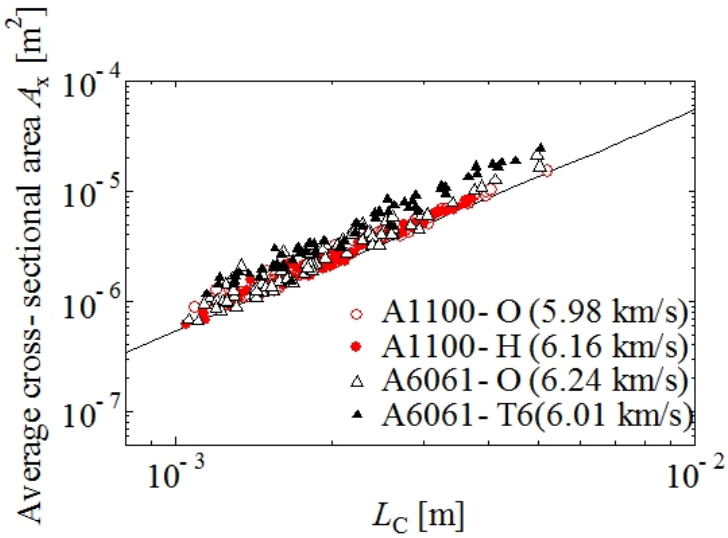

Fig. 3-21. JAXA/NIT impact tests. Average cross section of collected ejecta fragments

3.5 UKSPACE

Light-gas gun impact tests were performed at Unispace (Baron, 1997; McDonnell et al, 1998) on solar cell samples from the Hubble Space Telescope (HST) or EuReCA using ~500 μm glass bead projectiles at speed close to 5 km/s. Impact angle was set in the range 30° - 75° (test conditions and results summary are presented in Tab. 3-6).

All targets were completely perforated (cover glass, silicon and substrate) and hence test conditions were somewhat different from the ideal semi-infinite case. A significant part of debris cloud was therefore ejected downstream, thus reducing the amount of backscattered ejecta. Moreover, in some tests more than one projectile impacted the target at the same time, at some distance apart. It was difficult in these conditions to assess precisely the amount of ejecta and the angular distribution of fragments.

Test ID	*Target material*	d_p *(μm)*	v_p^* *(km/s)*	α *(°)*	*Comments*
33	HST solar cell	500	4.63	45	2 or 3 hits
37	HST solar cell	500	4.51	75	1 hit*
38	EuReCa solar cell	500	4.73	45	3 hits
39	EuReCa solar cell	500	4.66	75	1 hit

* Sabot impact on the stopper edge could have produced additional fragments

Tab. 3-6. Test performed on Hubble Space Telescope (HST) and EuReCa solar cell samples at UniSpace Kent (UK): impact conditions

Since targets were hit by more than one projectile, secondary damages observed on witness plates were quite scattered. Nevertheless, it was possible to recognize a clear variation in the density of impact features, along a line going upward from the base of the witness plate. For test no. 33, the maximum number of secondary impacts corresponded to an ejection angle of 60°. For test no. 38, the debris cone was widely open and the maximum number of secondary impacts occurred at an angle between 50° and 55°. For tests cases no. 37 and 39, secondary impacts were observed in a narrow band, corresponding to an ejection angle of about 80°-85°. The ricochet phenomena expected to occur for impact angles larger than 60° was observed only at angles greater than 75 °.

With the exception of test case 33 (no secondary damage larger than 200 μm were observed in this case), size of craters varied from 5 μm (optical resolution limit) to 750 μm. Even though such distribution is consistent with the one given by other experiments on brittle targets, the cumulative number is less than expected (about a factor of 2, this is due mainly to the perforation of the primary target as previously stated). Many small craters were circular in shape, with a depth to diameter ratio between 0.25 and 0.40 (this low ratio is consistent with impacts produced in copper and also with the low density of ejected silicon material). Large craters were irregular or oblong in shape (either sign of oblique impact or irregular shaped fragments). Velocity of ejecta was not measured, but morphology and geometry of secondary craters suggested an impact velocity speed exceeding 1 km/s.

The cumulative number of craters split in different size bins is shown in Tab. 3-7.

Crater equivalent diameter (μm)	*No. of craters Test no.33*	*No. of craters Test no.37*	*No. of craters Test no.38*	*No. of craters Test no.39*
>500	0	7	4	12
200-500	6	100	16	12
100-200	80	180	40	48
50-100	250	240	170	240
20-50	0	0	0	10000
10-20	0	0	0	21000
5-10	0	0	0	0

Tab. 3-7. Test performed on Hubble Space Telescope (HST) and EuReCa solar cell samples at UniSpace Kent (UK): cumulative number of craters per size

3.6 NASA

NASA has performed a number of impact tests over the years to study ejecta generation and effects on spacecraft. One study is described in Christiansen (1993), where a 0.2cm thick Al 3003-0 ejecta catcher was positioned 10cm in front of a variety of different bumper shield materials. A 1.27cm diameter hole was drilled in the center of the ejecta catcher, to allow the projectile to pass by the ejecta catcher without interference. All projectiles were 0.32cm diameter Aluminum 2017-T4 alloy spheres, impacting the target materials at nominally 6.8 km/s and at a 0^o impact angle (normal to the target surface).

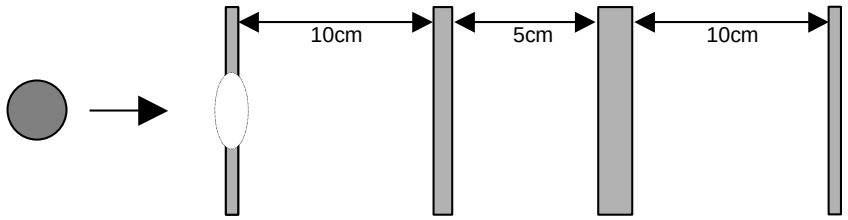

Fig. 3-22. Cross-section of NASA test setup

Table 3-8 provides data from these tests obtained by high-speed cameras and visual observations of the ejecta catcher. As indicated, no ejecta damage was evident from the aluminum mesh and Kevlar bumpers, and the ejecta expansion velocity was very low with these materials.

*Rank**	*Bumper Material*	*Ejecta Maximum Velocity (km/s)*	*Damage to ejecta catcher*
1	Aluminum mesh	2.1	No holes, no damage
2	Kevlar	2.4	No holes, no damage
3	Alumina/aluminum laminate	4.2	No holes, small scratches
4	Aluminum/graphite-epoxy laminate	3.9	A few small holes (<20)
5	35% SiC-Al composite	5.2	130 small holes (0.46mm max hole diameter), estimate largest secondary particle size is 0.2mm
6	Aluminum 6061-T6 alloy	6.7	Many holes > 1mm diameter

Tab. 3-8. Secondary ejecta characteristics for various bumper materials. Data from HVI of 0.32cm Al projectile at 6.8 km/s, normal impact, on 0.22 g/cm^2 bumpers. *Rank based on damage to ejecta catcher, with the highest rank resulting in the least amount of damage to the ejecta catcher.

NASA performed another ejecta study reported by Shephard and Scheer (1993). A number of

impact tests were performed to evaluate the consequences of secondary ejecta impacts on Space Station hardware, including electronic boxes, fluid and electrical umbilical lines, and antenna waveguides. Although these systems were damaged from secondary ejecta impacts, no failures of the hardware were observed.

4 Recommendations for experimental characterization of ejecta

This section provides recommendations on experimental methods for ejecta characterization, with the aim of setting common references for the comparison and utilization of data obtained by different facilities. This includes the identification of ejecta parameters to be measured during and after impact experiments, the selection of materials and configurations suitable to represent realistic spacecraft hardware, the definition of impact test conditions and a complete description of two benchmark cases for normal and oblique angle. Finally, procedures for data utilization are suggested to derive information on total ejecta mass, fragments spatial distribution and average velocity.

The content on this section is based but not limited to the ISO Working Document ISO/TC 20/SC 14 - FDIS 11227 [ISO, 2012].

4.1 Measurement objectives

Knowledge of the 3-D spatial mass-speed distribution, shape and ballistic coefficients of fragments in function of impact conditions and target parameters would in principle provide a full characterization of backscattered ejecta clouds. There is a variety of experimental techniques suitable for this scope, employing soft catchers, witness plates, photographic and X-ray imaging and indirect methods which allows a determination of the mass, momentum or energy of the fragments (Nysmith and Denardo, 1969; Wilbeck and Young, 1992). Some of these techniques have been described elsewhere in this report and used by researchers from ASI and JAXA.
However, full characterization of each secondary debris particle in the ejecta cloud (especially individual measurement of the velocity) is currently unfeasible and/or unpractical. Considering such limitations, and in accordance to the proposed ISO standard [ISO, 2012], it is suggested to set the following parameters as measurement objectives:

- **Total amount of back-scattered ejecta $M_{e,tot}$**
  $M_{e,tot}$ includes the mass of fragments belonging to both the target and the projectile:

$$M_{e,tot} = M_{e,target} + M_{e,proj} \qquad \text{Eq. 4-1}$$

  When comparing the ejecta mass emerging from different materials, only fragments coming from the target could be of interest. However, it should be considered that projectile ejecta are usually less than 1% of the total secondary debris mass and therefore negligible. Moreover, a comparison between the behavior of different targets could be done by fixing the projectile properties (material and impact conditions) during experimental activity.

- **Crater pattern and size distribution of craters on a witness plate facing the target**.
  The crater pattern left by secondary debris on a witness plate placed close to the target

provides information on the ejecta cloud bulk geometry (primarily the cone angle, see Fig. 1-2) as well as the number and size distribution of craters. These data give a raw estimate of the mass of individual fragments in the cloud. However, craters extension is not sufficient to univocally determine the velocity and size of the particles that caused the damage: in fact a crater of given size could be both produced by large and slow particles, as well as small and fast ones.

- **Average (or maximum) speed of ejecta.**
  As an option, the average (or maximum) speed of ejecta particles can be assessed using proper instrumentation (e.g. active sensors or high speed cameras) that provide a direct measure of the time of flight of secondary debris from the impact point on the target to the witness plate. Measurement of the individual velocity of particles is currently unfeasible and/or unpractical.

4.2 Experimental methods

4.2.1 Materials selection

The choice of materials regards the target from which secondary debris come as well as witness plates or catchers located close to the target to record information on ejecta particles.

a. Target materials

Criteria for materials selection are based on their representativeness of real space hardware and on the extent of their utilization in space (e.g. total area). However, material type, thickness (relative to projectile dimension), and surface conditions (e.g. roughness) as well as configuration (fabric, mesh versus solid plate, etc.) influences quantity and damage potential of secondary ejecta and therefore additional geometric information of target samples has to be taken into account.

The bulk of ejecta come from brittle materials (i.e. solar cells and glass windows), while the amount of secondary debris from aluminum alloys is more than two times lower. Furthermore, ageing of materials could contribute to increase with time the quantity of ejecta from solar panels [Myagkov et al, 2009]. However, the large presence of aluminum surfaces on orbit makes it necessary to account from aluminum ejecta.

It is suggested to consider the following:

- Aluminum alloy (AMG-6, Al6061-T6, Al7075-T6), representative of rocket bodies structures, skins of honeycomb sandwich panels and bumper panels on manned vehicles (>1000 m^2 on the ISS, thickness 0.08-0.2 cm);
- Aluminum alloy (AMG-6, Al1100-O, Al1100-H, Al6061-O, Al6061-T6) coated with

inorganic white paint, representative of the face-sheets of honeycomb sandwich radiator panels (>500 m^2 on the ISS, US segment, thickness 0.028 cm);

- Aluminum alloy (AMG-6, Al1100-O, Al1100-H, Al6061-O, Al6061-T6) covered by MLI thermal blankets, representative of surface panels and external equipment boxes;
- CFRP plates, representative of the face-sheets of honeycomb sandwich panels for spacecraft structures;
- Fused silica or quartz glass, representative of the cover-glass of solar cells and manned vehicles windows (outer panel thickness 10-14 mm);
- Solar cells assembly, consisting of relatively thin (~1mm) sandwiches made by (through-the-thickness): cover-glass, silicon cell, kapton.
- MLI coated with a protective thin layer of silicon (MAPATOX) becoming brittle after exposure to space.
- Thermal control paint on aluminum substrate (either on S/C components or on launcher bodies)

As a preliminary indication, the speed of secondary ejecta particles is much lower for fabrics than solid plates [Christiansen et al, 2010].

b. Witness plates and catchers

Witness plates or particles catchers are used to record information on ejecta fragments. The main difference between the two solutions is that catchers made by soft material (e.g. low density foams) in principle permit the recovery of almost intact fragments, while witness plates give only indirect information on ejecta properties based upon the characteristics of the resulting impact craters.

However, catchers require long manual operations to retrieve particles from the collector bulk material, whereas witness plates can be analyzed automatically by means of suitable imaging systems.

A comparative evaluation between witness plates and catchers for derive ejecta properties is discussed in [Francesconi et al, 2010]. Few impact experiments were conducted to evaluate the behavior of different catchers made of low density foams for industrial application such as thermal and acoustic insulation. Because of the extremely brittle nature of the foams, results were not satisfactory: ejecta fragments contributed to the global collapse of the catcher structure at every impact condition and recovery of fragments was not possible. On the contrary, useful information was retrieved by automatic analysis of the crater patterns left on metal witness plate (see section 4.2.3 for a description of witness plate analysis procedures).

4.2.2 Test conditions

The choice of test conditions should be based upon a reproducibility requirement, i.e. selected

experimental parameters should be achievable by most facilities in order to make the comparison of results easy.

The list below is just a minimum set of test conditions that every facility running ejecta experiments should consider to provide a common benchmark. Other test conditions for deepening the knowledge on ejecta phenomena and populating databases are recommended as well.

a. Projectile parameters

- Material: aluminum alloy (e.g. Al 6061-T6, Al 2024-T6, Al 2017, Al 1100)
- Shape and size: sphere, d_p = 0.1±0.01 cm diameter
- Impact velocity: v_p = 5.0±0.1 km/s
- Impact angle: α = 0°, α = 45° and α = 60° (TBC)

The execution of tests at non-zero impact angle is recommended in addition to normal impact. In fact, oblique impact is the only mean of not loosing fragments through the hole realized in the witness plate to make the projectile reach the primary target (especially when testing brittle targets, which typically produce narrow ejecta cones).

b. Target parameters

- Material: aluminum alloy (e.g. Al 6061-T6, Al 7075-T6)
- Size: a_x x a_y ≥ 50 mm x 50 mm
- Thickness: t ≥ 10 mm
- Fixture: threaded rods and bolts or clamps on the edges
- Back surface left free

Among the target material and impact conditions, the production of ejecta depends on the target thickness over projectile diameter ratio (t/d). To fix such degree of freedom, it is recommended to select semi-infinite targets (i.e. target with thickness sufficient to prevent formation of spall on the rear surface). However, if the behavior of specific spacecraft components is the major interest, the target thickness should be selected to be representative of the real flight hardware.
As an indication, thinner targets generate less damaging secondary ejecta than thicker ones [Christiansen et al, 2010].

c. Witness plate parameters

- Material: pure copper, annealed (e.g. C1100)
- Size (normal impact): w_x x w_y ≥ 200 mm x 200 mm, with central circular hole having diameter ϕ ≤ 30 mm
- Size (oblique impact): w_x x w_z ≥ 200 mm x w_z, with w_z greater than 4 times the later size

of the target (see Fig. 4-3)

- Position (normal impact): in front of the target and parallel to the target surface, at distance $S \leq 100$ mm
- Position (oblique impact): adjacent to one target edge and normal to the target surface
- Thickness: $t_W = 2$ mm
- Surface processing: chemical polishing
- Fixture: threaded rods and bolts or clamps on the edges
- Back surface left free

Surface roughness should be specified in test reports.

4.2.3 Benchmark cases

Following the above indications, two benchmark cases are recommended for comparing results on ejecta belonging to different test facilities.

In both cases, if brittle materials are used for targets, several spall fragments are generated and the target can be disrupted by the impact pressure. It is therefore recommended to protect the test specimen with a rubber sponge as shown in Fig. 4-1 [Sugahara et al, 2009].

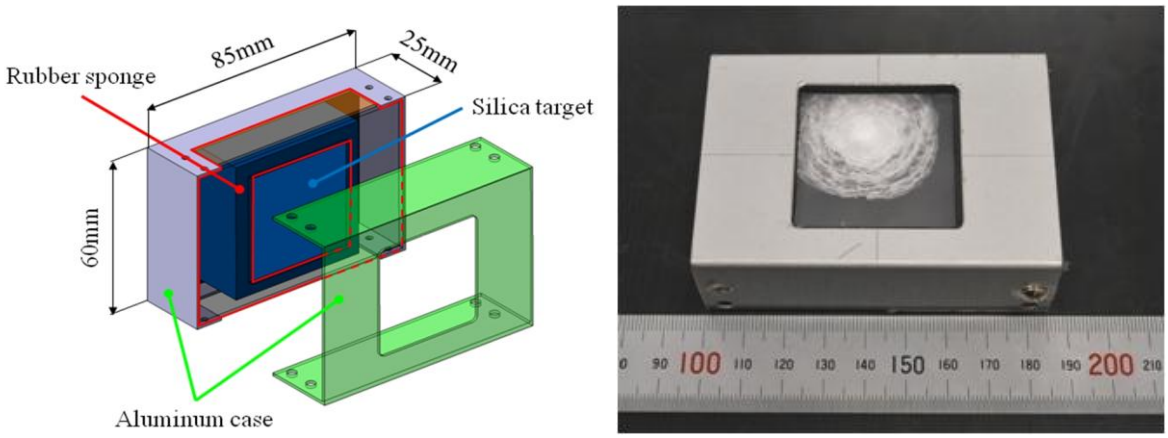

Fig. 4-1. Target holder for brittle materials [Sugahara et al, 2009]. Sizes are given as preliminary indication.

a. Normal Impact

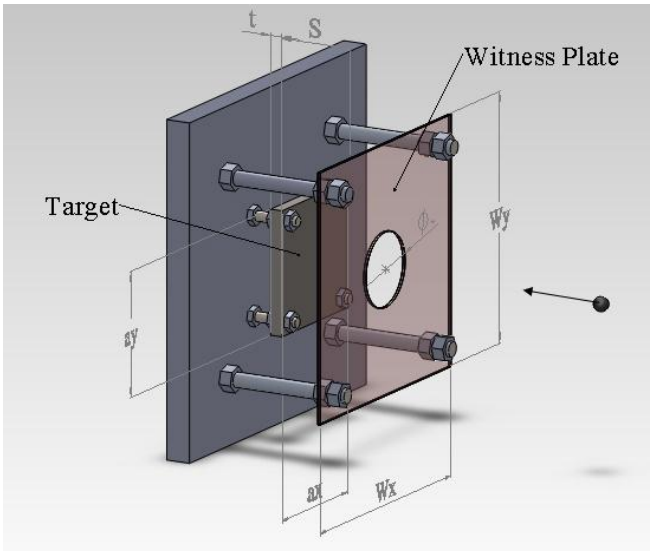

Fig. 4-2. Sketch showing the recommended setup for normal impact tests (benchmark #1). Interface with the impact facility is considered to vary from one facility to another.

To avoid deposit of dust coming from impact facility operations on the witness plate back face, a protecting screen (not shown in the figure) with a central hole having diameter ϕ could be placed uprange the witness plate (this could be useful to reduce uncertainty on witness plate mass after the test).

b. Oblique Impact

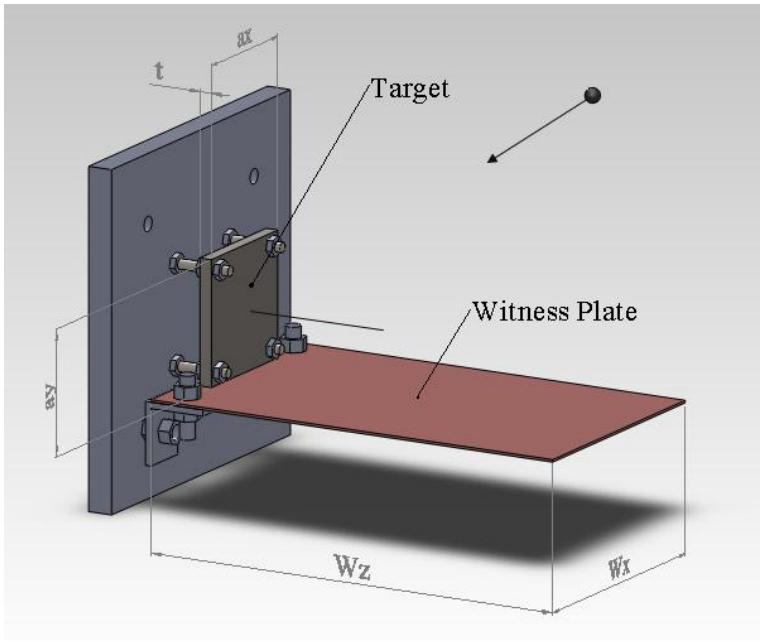

Fig. 4-3. Sketch showing the recommended setup for oblique impact tests (benchmark #2). Interface with the impact facility is considered to vary from one facility to another.

4.3 Data analysis

4.3.1 Total amount of back-scattered ejecta $M_{e,tot}$

$M_{e,tot}$ can be obtained by measuring the target and/or witness plate mass before ($M_{t,in}$ and/or $M_{wp,in}$) and after ($M_{t,fin}$ and/or $M_{wp,fin}$) the impact test. The total ejecta mass can be in fact related to the target and/or witness plate mass difference ($\Delta M_t = M_{t,in} - M_{t,fin}$ and/or $\Delta M_{wp} = M_{wp,fin} - M_{wp,in}$).

In both cases it is strongly recommended to specify the uncertainty in the ejecta mass estimation, considering that:

- The target mass after the test accounts for projectiles fragments that remain trapped within the impact crater (M_{trap}) and, depending on the impact facility used, dust can be deposited on the target surface ($M_{dust,t}$):

$$M_{e,tot} = \Delta M_t + M_{trap} + M_{dust,t} \qquad \text{Eq. 4-2}$$

  On one hand, M_{trap} is usually less than 1% of the secondary debris mass and therefore can be neglected. On the other hand, depending on the facility used, $M_{dust,t}$ can be a significant part of ΔM_t, especially when small quantities of ejecta are produced (e.g. ductile targets hit by small projectiles). In this case, it is suggested to experimentally estimate $M_{dust,t}$ by running few calibration experiments in which empty sabots with no projectile inside are launched at the same impact conditions selected for the real testing activity. Since no projectile hits the target, in such experimental condition $M_{dust,t}$ is equal to ΔM_t.

- In case of normal impacts, the witness plate cannot capture fragments ejected back within the plate central hole (M_{loss}) and the plate back face can be contaminated by dust consequent to impact facility operations ($M_{dust,wp}$):

$$M_{e,tot} = \Delta M_{wp} + M_{loss} - M_{dust,wp} \qquad \text{Eq. 4-3}$$

  On one hand, M_{loss} can be significant especially when the target is brittle and its estimation might be difficult. On the other hand, $M_{dust,wp}$ can be nearly null if a protecting screen is used uprange the witness plate.

The different estimations of $M_{e,tot}$ obtained by Eq. 4-2 and Eq. 4-3 must be compatible within their uncertainty ranges. However, It's worth to notice that both M_{loss} and $M_{dust,wp}$ (Eq. 4-3) become negligible in case of oblique impact. It therefore seems that measuring the witness plate mass difference ΔM_{wp} in case of oblique impact could provide the best estimation of the total ejecta mass.

4.3.2 Witness plates craters

Analysis of the damage pattern on witness plates (position, number and size of craters) provides data on the bulk geometry of the ejecta cloud. If witness plates inspected with some reproducible technique (e.g. by a medium-power optical microscope), craters analysis can benefit from automated pattern recognition procedures, see Sugahara et al [2009], Francesconi et al [2010].
To avoid erroneous craters identifications due to scratches or imperfections of the plate and to reduce the uncertainty of the image processing results, it is suggested to use chemically polished witness plates and to compare high resolution plates images acquired before and after the impact experiment.

It is then recommended to sort the impact craters in the following classes of equivalent diameter. The resolution of the craters pattern analysis system should be specified as well.

- between 0.025 mm and 0.05 mm (mainly from the ejecta cone);
- between 0.05 and 0.1 mm (mainly from the ejecta cone);
- between 0.1 and 1 mm (mainly from spall);
- > 1 mm (from spall).

The size distribution of craters provides only a raw estimate of the mass of individual fragments in the cloud, since craters extension is not sufficient to univocally determine the velocity and size of the particles that caused the damage. Additional information is therefore requested, e.g. an estimation of fragments velocity normal to the witness plate face (see section 4.3.3) and a procedure using well-established empirical equations relating craters extension to the size and speed of impacting particles (see section 4.3.4).

4.3.3 Ejecta speed

The velocity of ejecta fragments can be evaluated by analyzing pictures of high-speed video camera systems looking at the impact event and/or with adequate point sensors which provide a measure of the ejecta time-of-flight from the primary target to the witness plate. However, the employment of both systems has significant drawbacks which could make difficult and/or inaccurate the ejecta speed assessment:

- High speed camera systems can in principle provide combined information on velocity and size of individual fragments. Nevertheless, automatic tracking of particles within the ejecta cloud is a difficult task and consequent trajectory/speed evaluation can be affected by large errors.
- Time-of-flight measurements can be achieved by sensors detecting ejecta impacts on the witness plate and triggered by the projectile impact on the primary target. Possible alternatives are given by contactless impact flesh detectors looking at both the target

and the witness plate and/or impact sensors (e.g. strain gauges, accelerometers, PDVF films, etc.) located on the witness plate. However, in both cases, it should be considered that ejecta clouds are complex structures in which particles of various size travel in different directions and have a wide range of velocities. Hence, time-of-flight sensors can provide only an estimation of the average (or maximum) ejecta cloud speed and this could give a misleading picture of the phenomenon under investigation.

In both cases, it is recommended to assess and specify the uncertainty on the speed estimation.

4.3.4 Procedure for deriving ejecta mass distribution in the cloud

Ejecta mass (size) distribution can be obtained if the following information is available:

- Witness plates craters number and size (see section 4.3.2);
- Ejecta fragments speed (at least average or maximum, see section 4.3.3);
- Empirical equations relating craters extension to the size and speed of impacting particles, in the form of Eq. 4-4:

$$D_C = f\,(d_p,\, v_p,\, \alpha,\, projectile\ material,\, target\ material) \qquad \text{Eq. 4-4}$$

In the above equation, D_c is the crater equivalent diameter, d_p and v_p are the projectile's diameter and speed, α is the impact angle. Projectile and target material normally appears in the equation through density and/or other specific empirical coefficients.

When the three pieces of information above are available, the analysis of the witness plate damage pattern gives a measure of the equivalent diameter $D_{C,j}$ of the *j*-th crater larger than 0.025 mm and knowledge of the *j*-th crater position on the witness plate provides an estimation of the impact direction and hence the angle α_j.
Furthermore, proper instrumentation (high-speed camera system and/or impact sensors) provides the speed of *j*-th ejecta fragment $v_{e,j}$ and/or the average velocity of the cloud $v_{e,avg}$.
Finally, if empirical crater equations such as Eq. 4-4 are available from the technical literature, it is therefore possible to estimate the mass of the *j*-th fragment $m_{e,j}$ and/or the average mass $m_{e,avg}$ of the particles in the cloud:

$$m_{e,j} = f^{-1}\left(D_{c,j}, v_{e,j}, \alpha_j\right) \qquad \text{Eq. 4-5}$$

$$m_{e,avg} = avg\left[f^{-1}\left(D_{c,j}, v_{e,avg}, \alpha_j\right)\right] \qquad \text{Eq. 4-6}$$

In both cases, it is recommended to assess and specify the uncertainty on the fragments mass estimation.

Uncertainty depends on the imaging system used to analyze craters onto witness plates, the accuracy of the ejecta speed estimations and the reliability of empirical equations describing craters size as a function of fragments speed and mass. It should be reminded that the validity of such equations is often limited to certain experimental ranges and in general holds for spherical particles only.

5 Ejecta database

The section summarizes the information that should be contained in a database describing the behavior of material upon HVI with respect to their ejecta-production capability, with the scope of providing users with data to predict/reduce the environment pollution from secondary fragments.

The database will initially be populated with public data, provided in a later version of this report, and could be regularly updated as soon as new tests or simulation results become available.

5.1 Test setup

The following information should be provided:

- Target category (e.g. brittle or ductile)
- Target material, thickness, size and mass (with uncertainty) before impact
- Witness plate (or catcher) material, size, mass (with uncertainty) and surface finish before impact
- Sketch showing the relative position (standoff and angle) between target and witness plate (or catcher) as well as their fixture
- Description of instrumentation for ejecta speed measurement (if any)

In case of numerical simulations, additional information is requested:

- Target material models, mesh type (SPH, Euler, etc.) and resolution
- Projectile material models, mesh type (SPH, Euler, etc.) and resolution
- Witness plate material models, mesh type (SPH, Euler, etc.) and resolution

5.2 Test conditions

The following information should be provided:

- Projectile material, shape, size, impact speed (with uncertainty) and impact angle

5.3 Experimental/numerical results

The following information should be provided:

- Total ejecta mass (with uncertainty)
- WP high resolution picture
- Cone angle (with uncertainty)

- Number of WP craters in size bins
- Number of retrieved fragments in size bins, including aspect ratio
- Ejecta cloud maximum (and/or average) speed (with uncertainty)

6 Acronyms and Abbreviations

AI	Action Item
Al	Aluminum
ASI	Agenzia Spaziale Italiana (Italian Space Agency)
BLE	Ballistic Limit Equation
CEA	Atomic Energy Commission (France)
CEG	Centre d'Etudes de Gramat
CFRP	Carbon Fiber Reinforced Polymer
CISAS	Interdepartmental Center for Space Studies and Activities
CNES	National Center for Space Studies
DLR	Deutsche Zentrum für Luft- und Raumfahrt (German Aerospace Center)
EMI	Ernst-Mach Institute
ESA	European Space Agency
EVA	extravehicular activity
GEO	Geostationary Earth Orbit
HST	Hubble Space Telescope
HVI	Hypervelocity Impact
IADC	Interagency Space Debris Coordination Committee
ISAS	Institute of Space and Astronautical Science
ISO	International Standards Organization
ISS	International Space Station
ISTC	International Science and Technology Center
JAXA	Japan Aerospace Exploration Agency
JSC	Johnson Space Center
KIT	Kyushu Institute of Technology
LDEF	Long Duration Exposure Facility
LEO	Low Earth Orbit
M/OD	Meteoroids and Orbital Debris
MMOD	Micrometeoroid and Orbital Debris
MASTER	Meteoroid and Space Debris Terrestrial Environment Reference
MLI	Multilayer Insulation
NASA	National Aeronautics and Space Administration
NIT	Nagoya Institute of Technology
ONERA	Office National d'Études et de Recherches Aérospatiales
ORDEM	Orbital Debris Environment Model (NASA)
ROSCOSMOS	Russian Federal Space Agency
S/C	Spacecraft
SiO2	Silicon Dioxide
SPH	Smoothed-Particle Hydrodynamics
TU Braunschweig	Technische Universität Braunschweig
UV	UltraViolet
WG	Working Group
WP	Witness Plate

7 References

Anderson C.E. Jr, Trucano T.G, Mullin S.A. (1990). Debris cloud dynamics. Int. J. Impact Engng. 9-1, 89-113.

Arakawa M. et al (1995), Ejection velocity of ice impact fragments. Icarus 118, pp 341-354.

Asada N. (1985) Fine fragments in high-velocity impact experiments. JGR 90-B14, pp 12445-12453.

Barge P. and Pellat R. (1993) Mass spectrum and velocity dispersion during planetesimal accumulation: II-Fragmentation. Icarus 104, pp 79-96.

Bariteau M. and J.C. Mandeville (2001). A modelling of ejecta as a space debris source, ESA SP-473, 321-326.

Bariteau M., J.C. Mandeville, F. Schäfer (2001). Ejecta production mechanism on painted surfaces, ESA SP- 473, p.249-251

Bariteau M. (2001) Prolifération des débris orbitaux: production et évolution des particules secondaires, Thèse ENSAE, Toulouse 2001

Baron (1997), private communication to J.C. Mandeville.

Bess T.D. (1975) Mass distribution of orbiting man-made space debris. NASA TN D-8108.

Borisov B.S, Garkusha V.I, Korsun A.G, Sisov A.A, Khomich T.M, Tverdokhlebova E.M. (2010). Investigation of characteristics of electrical discharge at metal-dielectric surfaces of ISS. In Proc. Conf. Information technologies in science, engineering, and education devoted to 50th Anniversary of the first flight of a man in space – Yu.A.Gagarin. A.M. Prokhorov Academy of Engineering Sciences. Pitsunda, Abkhazia, 20 Sept. - 1 Oct. 2010.

Caswell R.D, McBride N, Taylor A.D. (1995). Olympus end of life anomaly – a Perseid meteoroid impact event? Int. J. Impact Engng, 17, 139- 150

Christiansen E.L., Cour-Palais B.G., Friesen L.J. (1999). Extravehicular Activity Suit Penetration Resistance, International Journal of Impact Engineering, Vol. 23, pp. 113-124.

Christiansen, E.L. (1987). Evaluation of Space Station Meteoroid/Debris Shielding Materials, Eagle Engineering Report No. 87-163.

Christiansen, E.L. (2003). Meteoroid/Debris Shielding, NASA Technical Publication, NASA/TP-2003-210788.

Christiansen, E.L. et al. (2009). Handbook for Designing MMOD Protection, NASA TM-2009-214785.

Christiansen E.L., Nagy K, Hyde J. (2010) NASA secondary ejecta status. In Proc. 28th IADC Meeting. March 2010, Trivandrum, India

Cohen L.J. (1995). A debris cloud cratering model. Int. J. Impact Engng. 17/1-3, 229-240.

Corvonato E., Destefanis R., Faraud M. (2001). Integral model for the description of the debris cloud structure and impact, Int. J. Impact Engng. 26/1-10, 115-128

Cour-Palais B.G. (1982). Hypervelocity impact investigation and meteoroid shielding experiments related to Apollo and Skylab. Orbital Debris. NASA CP 2360.

Dohnanyi J.S (1967). Collisional models of asteroids and their debris. Symposium n.33 of IAU, in Physics and Dynamics of Meteors, (Kresak and Millmaneds), Reidel Publishing Company, Dordrecht, Holland.

Drolshagen G, Nehls T and Noomen R. (2009) The small debris population in the GEO belt. In Proc. 5th Europ. Conf. Space Debris. 30 March – 2 April 2009, ESOC, Darmstadt, Germany

Eichhorn G. (1975) Measurement of the light flash produced by high velocity particle impact. Planet. Space Sci.,23, pp.1519-1525.

Eichhorn G. (1976), Analysis of the hypervelocity impact process from impact flash measurements, Planet Space Sci., 24, 771.

Finnegan S.A, Pringle J.K, Atwood A.I, Heimdahl O.E.R, Covino J. (1995). Characterization of impact-induced violent reaction behavior in solid rocket motors using a planar motor test model. Int. J. Impact Engng. 17/1-3 311-322.

Francesconi A., C. Giacomuzzo and L. Barilaro (2010). A method to assess the average properties of spacecraft ejecta from hypervelocity impact, Proc. of the 11 th Hypervelocity impact symposium.

Francesconi A, Giacomuzzo C, Barilaro L, Segato E (2010). Number, size and speed distribution of particles ejected from spacecraft surfaces during hypervelocity impact, in proc. 61st ARA Meeting.

Frisch W. (1991), Hypervelocity impact experiments with water ice target, in Hypervelocity Impacts in Space, J.A.M. McDonnell editor, pp 7-14.

Fujiwara A., Kamimoto G. and Tsukamoto A. (1977), Destruction of basaltic bodies by high-velocity impact, Icarus 31, pp 277-288.

Fujiwara A. and A. Tsukamoto (1980), Experimental study on the velocity of fragments in collisional breakup, Icarus 44, 142-153.

Gault D.E. and Heitowit E.D. (1963), The partition of energy for hypervelocity impact craters formed in rocks, Proc. of the 6th Hypervelocity Impact Symposium

Gault D.E., Shoemaker E.M. and Moore H.J. (1963), Spray ejected from the lunar surface by meteoroid impact, NASA TN D-1767.

Gault D.E. and Wedekind J.A. (1969) The destruction of tektites by micrometeoroid impact, Journal of Geophysical Research, Vol. 74, No 27.

Gault D.E., Hörz F. and Hartung J.B. (1972), Effects of microcratering on the lunar surface, Proc. IIIrd Lunar Sci. Conf., vol. 3.

Gault D.E. (1973), Displaced mass, depth, diameter, and effects of oblique trajectories for impact craters formed in dense crystalline rocks, The Moon 6, pp.32-44.

Hill D.C. (1990). The micrometeoroid impact hazard in space: techniques for damage simulation by pulsed lasers and environmental modelling, PhD. Thesis, University of Kent at Canterbury, UK.

ISO/TC 20/SC 14 - FDIS 11227 (2012). Space Systems – Test procedures to evaluate spacecraft material ejecta upon hypervelocity impact

Kessler D.J. and Cour-Palais B. (1978) Collision frequency of artificial satellites: creation of debris belt. Journal of Geophysical research, 83, A6, 2637-2644

Kessler D.J. (1990) Collision probability at low altitudes resulting from elliptical orbits. Adv. Space Res. 10/3-4, 393 – 396.

Kessler D.J, Zhang J, Matney M.J, Eichler P, Reynolds R.C, Anz-Meador P.D, and Stansbery E.G. (1996) A computer based orbital debris environment model for spacecraft design and observations in low Earth orbit. NASA TM-104825.

Kolesnikov E.K, Chernov S.V. (2009) On the possibility of long time existence of man-made microparticles injected on oblong elliptic orbits with low perigee altitude in the near Earth space. In Proc. 5th Europ. Conf. on Space Debris. 30 March – 2 April 2009, ESOC, Darmstadt, Germany.

Korsun A.G. (2010) Prediction of liquid propulsion impact on electric discharge processes at the surface of the International space station. In Proc. Space Propulsion Conf., San Sebastian, Spain,

3-6 May 2010.

Korsun A.G. (2010) Electric discharge processes in the plasma environment of the ISS generated by high voltage solar arrays. In Proc. Conf. Information technologies in science, engineering, and education devoted to 50th Anniversary of the first flight of a man in space – Yu.A. Gagarin. A.M. Prokhorov Academy of Engineering Sciences. Pitsunda, Abkhazia, 20 Sept. – 1 Oct. 2010.

Lambert M, Schneider E. (1997). Hypervelocity impacts on gas filled pressure vessels. Int. J. Impact Engng 20/6-10, 491-498.

Lange M.A, Ahrens T.J. and Boslough M.B. (1984). Impact cratering and spall failure of Gabbro. Icarus 58, pp 383-395.

Lecomte C. (1963), Particules secondaires émises lors d'impacts à grande vitesse, Notice N29/63, Institut Franco-Allemand de Recherches de Saint-Louis.

Loupias C. (1996), Private comunication to J.C. Mandeville.

Maki K. et al (2002). Detection of microwave emission in hypervelocity impact on aluminium. In Proc. Asia-Pacific Microwave Conference, Kyoto, pp.1327-1330

Mandeville J.C. and Rival M. (1996), Enhanced Debris/Micrometeoroid Environment Models and 3-D Tools - Technical Note TN2 : Review and Selection of a Model for Ejecta Characterization, Partial Report 452200/01, ONERA-CERT Toulouse.

Mandeville J.C, Perrin J.M, Vuillemin A. (2001). Space borne photometry perturbations from solar light scattered by debris. In Proc. 3rd Europ. Conf. on Space Debris, ESOC, Darmstadt, Germany, 19-21 March 2001.

Mandeville J.C., M. Bariteau (2004). Contribution of secondary ejecta to the debris population. Adv. Space Res. 34, 944-950.

Mandeville J.C., Kitazawa Y., Akahoshi Y., Matsumoto H. (2010). Current status on CD11227 Test procedures to evaluate S/C material ejecta upon HVI, ISO/TC20/SC14 Meeting, BSI London, May 10-14, 2010.

McDonnell J.A.M, McBride N. and Gardner D.J. (1997). The Leonid meteoroid stream: spacecraft interactions and effects. In Proc. 2nd Europ. Conf. on Space Debris, Darmstadt 1997, pp.391-396

McDonnell J.A.M. et al. (1998) Meteoroid and debris flux and ejecta models, Final report ESA contract 1887/96NL/JG, CR 4252.

McKnight D.S. (1991). Determination of initial break-up conditions, J. Spacecraft and Rockets 28-

4, July-August.

McKnight D. and Edelstein K.S. (1992), Analysis of Shuttle window impact data, in Hypervelocity impacts in space, ed. McDonnell J.A.M., publ. Univ. of Kent at Canterbury.

Melin R.W. (1990). Hypervelocity impact testing of heat pipe samples. Int. J. Impact Engng 10/1-4, 389-401.

Meshcheryakov S.A. (2009). Analytical formulas for evaluation of meteoroid distributions in the near-Earth space. In proc. 5th Europ. Conf. on Space Debris, ESOC, Darmstadt, Germany, 29 March-3 April 2009.

Michel Y. et al. (2005). Damaging and ejection processes during HVI on brittle targets. Proc. 4 th European Conference on Space Debris, ESA SP-587, 2005.

Michel Y. et al. (2006), Damages and matter ejection during HVI on brittle structures: implications for space environment, 10th ISME proceedings, Collioure, France.

Michel Y, Chevalier J.M, Durin C, Espinosa C, Malaise F, Barrau J.J. (2006) Hypervelocity impacts on thin brittle targets: experimental data and SPH simulations. Int. J. of impact Engng 33, 441-451

Michel Y. et al. (2006), SPH modelling of glasses behaviour under shock loadings : application to matter ejection on thin targets, J. Phys. IV ..

Moussi A, Drolshagen G, McDonnell J.A.M, Mandeville J.C, Kearsley A. (2005) Results of impact analysis on HST service mission 3B solar arrays. In Proc. 4th Europ. Conf. on Space debris. ESOC, Darmstadt, Germany, 18-20 April, 2005.

Moussi A, Drolshagen G, McDonnell J.A.M, Mandeville J.C, Kearsley A.T. and Ludwig H. (2005) Hypervelocity impacts on HST solar arrays and the debris and meteoroids population. Adv. Space Res., 35:1243–1253

Myagkov N.N, Valiev H.H, Yanovsky Y.G, Kornev Y.V, Yumashev O.B, Rebrikov V.N. (2009) Investigation of the nanostructures on solar cells exposed on orbital space station MIR. In Proc. 5th Europ. Conf. on Space Debris. 30 March – 2 April 2009, ESOC, Darmstadt, Germany

Myagkov N.N. (2009). On bunching of orbital debris microparticles in circular and elliptic orbits. In Proc. 5th Europ. Conf. on Space Debris. 30 March – 2 April 2009, ESOC, Darmstadt, Germany

Nishida M, Kato H, Kuzuya K, Hayashi K and Hasegawa S. (2010) Effects of Different Series Aluminum Alloys and Their Heat Treatments on Crater Formation and Ejecta Composition. In Proc. 29th International Congress on High-Speed Imaging and Photonics, B12-1-6.

Nysmith C.R. and B.P. Denardo (1969). Experimental investigation of the momentum transfer associated with impact into thin aluminium targets. NASA TN-D-5492.

O'Donnell R.G. (1991). An investigation of the fragmentation behaviour of impacted ceramics. Journal of Materials Science Letters 10, pp 685-688.

O'Keefe J.D. and Ahrens T.J. (1987). The size distribution of fragments ejected at a given velocity from impact craters. Int.J. Impact Engng. 5, pp 493-499.

Oberbeck V.R. and Morrison R.H. (1976). Candidate areas for in situ ancient lunar materials, Proc.Lunar Sci. Conf. 7th, pp 2983-3005.

Oswald M, Stabroth S, Wiedemann C, Wegener P, Martin C, Klinkrad H. (2005) Upgrade of the MASTER Model , ESA, Institute of Aerospace systems.

Paul K.G. (1997). Ejecta clouds from hypervelocity collisions as seen by the LDEF interplanetary dust experiment. Adv. Space Res. 20-8, p.1545.

Piekutowski A.J. (1987). Debris clouds generated by hypervelocity impact of cylindrical projectiles with thin aluminum plates, Int.J.Impact Engng. 5/1-4, 509-518.

Piekutowski A.J. (1990). A simple dynamic model for the formation of debris clouds. Int.J.Impact Engng. 10/1-4, 453-471.

Piekutowski A.J. (1993) Characteristics of debris clouds produced by hypervelocity impact of aluminum spheres with thin aluminum plates. Int.J.Impact Engng 14/1-4, 573-586.

Piekutowski A.J. (2001). Debris clouds produced by the hypervelocity impact of nonspherical projectiles. Int.J.Impact Engng 26/1-10, 613-624.

Polanskey C.A. and Ahrens T.J. (1990). Impact spallation experiments: fracture patterns and spall velocities. Icarus 87, pp.140-155.

Putzar R, Schaefer F, Lambert M. (2008). Vulnerability of spacecraft harnesses to hypervelocity impacts, Int. J. Impact Engng 35-12, 1728-1734.

Rival M, Mandeville J.C. and Durin C. (1996). Impact phenomena on brittle materials : analysis of 1μm to 1mm impact features on solar arrays. Adv. Space Res. 20-8, 1451-1456.

Rival M., J.C. Mandeville (1999), Modelling of ejecta produced upon hypervelocity impacts, Space debris 1, 45-57.

Schäfer F. and Schneider E., (1997). Hypervelocity mpacts on Solar Cells, EMI-Report No.HVISC-001.

Schafer F.K, Ryan S, Lambert M, Putzar R. (2008). Ballistic limit equation for equipment placed behind satellite structure walls. Int. J. Impact Engng 35-12, 1784-1791.

Schneider E. (1975). Impact ejecta exceeding lunar escape velocity. The Moon 13-1/2/3.

Schneider E. and Stilp A. (1993). Meteoroids/Debris simulation at EMI: Experimental methods and recent results, Proc. 1st European Conference on Space Debris, ESA SD-01, pp.401-404.

Schneider E., (1997), Private communication.

Schonberg W. (1989), Characterizing the damage potential of ricochet debris due to an oblique HVI, AIAA 89-1410 CP, pp 2180.

Schonberg W.P., Taylor R.A. (1990). Exterior spacecraft subsystem protective shielding analysis and design. J. Spacecraft and Rockets, 29, 267-274

Schonberg W.P. (2001). Characterizing Secondary Debris Impact Ejecta, Int. J. of Impact Engng., 26, 713-724

Seebaugh W.R. (1977). A dynamic crater ejecta model. Impact and Explosion Cratering, Pergamon Press (Roddy, Pepin and Merrill editors), pp 1043-1056.

Semkin N.D, Voronov K.E, Piyakov A.V, Novikov L.S. (2009). Ion's formation and photo issue at interaction of high-speed dust particles with optical glass. In Proc. 5th Europ. Conf. on Space Debris, 30 March – 2 April 2009, ESOC, Darmstadt, Germany.

Shephard G.L.Y. and Scheer, S.A. (1993). Secondary debris impact damage and environment study, International Journal of Impact Engineering, Vol.14, pp.671-682.

Shutov V.I. and Zheltov S.Y. (2010). Investigation of astrosols in near earth space. ISTC project 3412 Final report, GosNIIAS, Moscow.

Siguier J.M. and J.C. Mandeville (2007). Test procedures to evaluate spacecraft materials ejecta upon hypervelocity impact, Proc. ImechEvol 221 Part G: J. Aerospace Engineering.

Stilp A.J, Hohler V, Schneider E, Weber K. (1990). Debris cloud expansion studies. Int. J. Impact Engng 10/1-4, 543-553.

Stilp A.J, Weber K. (1997). Debris clouds behind double-layer targets. Int. J. Impact Engng 20/6-10, 765-778.

Stöffler D., Gault D.E., Wedekind J. and Polkowski G. (1975). Experimental hypervelocity impacts into quartz sand : distribution and shock metamorphism of ejecta. Journal of Geophysical Research, 80-29.

Stump W.R., Christiansen E.L. (1986). Secondary impact hazard assessment. Report No. 86-128, Eagle Engineering Inc., Houston, Texas.

Su S.Y. (1990). The velocity distribution of collisional fragments and its effect on future space debris environment. Adv. Space Res.10-3/4, pp (3) 389-392.

Sugahara K, Aso K, Akahoshi Y, Koura T, and Narumi T. (2009) Intact Measurement of Fragments in Ejecta due to Hypervelocity Impact, In Proc. 60th International Astronautical Congress, IAC-09-A6.3.06, October 2009.

Svedhem H. and Pedersen A. (1992). Behaviour of ejecta particles and generated plasma at hypervelocity impacts. Hypervelocity impacts in space, ed. McDonnell J.A.M., Univ. of Kent at Canterbury.
Tanaka K. et al. (2008) Hypervelocity crater formation in aluminum alloys at low temperatures. Int. J. Impact Engng. 35, 1821–1826

Takano T, Murotani Y, Toda Y. et al., (2000). Microwave generation due to hypervelocity impact. In Proc. 51st IAF Congress, IAA-00-IAA.6.5.07, Brazil.

Takano T, Murotani Y, Maki K. et al. (2002). Microwave emission due to hypervelocity impacts and its correlation with mechanical destruction. J.Appl.Phys. 92-9,5550-5554.

Takano T, Maki K, Soma E, Ohnishi H, Ishii K, Chiba S, Fujiwara A, and Yamori A. (2005). Material Dependence Of Microwave Emission Due To A Hypervelocity Impact. In Proc. 4th Europ. Conf. on Space Debris, Darmstadt, Germany, 18-20 April 2005.

Wilbeck J.S. and R.P. Young (1992). Experience with techniques for characterizing debris generated during hypervelocity impact testing. AIAA 92-1586.

Woodward R.L. et al (1994). A study of fragmentation in the ballistic impact of ceramics. Int. J. Impact Engng., Vol.15-5, pp 605-618.

Xu Y-L, Christiansen E, Hyde J, Matney M, and Prior T (2011). Simulation of Micron-Sized Debris Populations in Low Earth Orbit. NASA Orbital Debris Quarterly Newsletterl 15-2, April 2011.